The Influence of Surface Roughness on Post-Critical Flow Over Circular Cylinders Revisited

Anil Pasam[1,2,3]†**, Daniel Tudball Smith**[1,2,3]**, John D. Holmes**[4]**, David Burton**[1,2,3] **and Mark C. Thompson**[1,2,3]

[1]Monash Wind Tunnel Research Platform (MWTRP)

[2]Fluids Laboratory for Aeronautical and Industrial Engineering (FLAIR)

[3]Department of Mechanical and Aerospace Engineering, Monash University, Clayton, VIC 3800, Australia

[4]JDH Consulting, Australia

(4 October 2023)

This work investigates the effect of surface roughness on cylinder flows in the post-critical regime and re-examines whether the Roughness Reynolds number (Re_{k_s}) primarily governs the aerodynamic behaviour. It has been motivated by limitations of many previous investigations, containing occasionally contradictory findings. In particular, many past studies were conducted with relatively high blockage ratios and low cylinder aspect ratios. Both of these factors appear to have non-negligible effects on flow behaviour, and particularly fluctuating quantities such as the standard deviation of the lift coefficient. This study employs a 5% blockage ratio and a span-to-diameter ratio of 10. Cylinders of different relative surface roughness ratios (k_s/D), ranging from 1.1×10^{-3} to 3×10^{-3}, were investigated at Reynolds numbers up to 6.8×10^5 and Re_{k_s} up to 2200. It is found that the base pressure coefficient, drag coefficient, Strouhal number, spanwise correlation length of lift, and the standard deviation of the lift coefficient are well described by Re_{k_s} in post-critical flows. However, roughness does have an effect on the minimum surface pressure coefficient (near separation) that does not collapse with Re_{k_s}. The universal Strouhal number proposed by Bearman (1984) appears to be nearly constant over the range of Re_{k_s} studied, spanning the sub-critical through post-critical regimes. Frequencies in the separating shear layers are found to be an order of magnitude lower than the power law predictions for separating shear layers of smooth cylinders.

Key words: Post-critical flow, Cylinder wakes, Drag crisis, Rough cylinders, Roughness Reynolds number, Bluff Body flows.

---

† Email address for correspondence: anil.pasam@monash.edu

1. Introduction

For more than a century, the flow over circular cylinders has garnered the attention of fluid dynamics researchers. This is due to a combination of their geometric simplicity and axisymmetry, and their relevance to real-world applications. A host of studies on smooth circular cylinders has helped advance our understanding of how the aerodynamic forces and wake change as the Reynolds number is varied over a wide range. However, engineering structures seldom have perfectly smooth surfaces due to factors such as imperfections in surface finish, paint, corrosion, etc. At Reynolds numbers of $\mathcal{O}(10^5)$ and above – a range of considerable relevance to many applications – the surface roughness has a strong influence on flow separation and the wake, and in turn the lift and drag. This motivates further study of the flow over cylinders focusing on the effects of surface roughness, also noting that this Reynolds number range has been difficult to explore in practice with standard wind-tunnel based experiments. Therefore, a reliable, consistent, and comprehensive data set addressing these areas is necessary to unravel how the flow behaviour and underlying flow physics vary over this crucial range.

Broadly, the flow over circular cylinders can be classified into sub-critical, critical, super-critical, and post-critical regimes (Roshko (1961); Achenbach (1971); Güven *et al.* (1980)). These regimes are represented schematically in figure 1. They reflect key changes in the location of turbulent transition in the separating shear layer or boundary layer as the Reynolds number ($Re = U_\infty D/\nu$, with U_∞ the free-stream velocity, D the cylinder diameter, and ν the kinematic viscosity) is increased. The regimes can also be identified by the variation of the drag coefficient, C_D. In sub-critical flow ($10^4 \lesssim Re \lesssim 10^5$ for a smooth cylinder), the transition to turbulence occurs in the shear layers in the near wake of the cylinder, and C_D remains fairly constant with increasing Reynolds number. As the Reynolds number is increased further ($Re \sim \mathcal{O}(3 - 4 \times 10^5)$), this transition moves upstream to occur in the separating shear layers very close to the separation point. When transition occurs in this key region, it allows the separated shear layers to reattach to the surface and separate at a later position further towards the rear of the cylinder. This separation zone near reattachment, marked by laminar separation, transition to turbulent flow and reattachment, is known as the *Laminar Separation Bubble* (LSB).

The formation of the LSB delays the eventual final separation of the boundary layer allowing the pressure to recover and hence results in a significant drop in C_D from that in the sub-critical state. It is in this range that the minimum C_D with respect to Reynolds number is observed. Further increase in Reynolds number ($Re \gtrsim 4 \times 10^5$ for a smooth cylinder) causes upstream movement of the transition in the boundary layer that results in intermittent and asymmetric formation of the LSB followed by no LSB and thus leads to increasing C_D in the super-critical regime. In the post-critical regime ($Re \gtrsim 6 \times 10^6$ for a smooth cylinder), the transition to turbulence in the boundary layer occurs sufficiently upstream on the cylinder surface that C_D becomes nearly insensitive to Reynolds number. However, the higher momentum in the turbulent boundary layer enables it to remain attached for longer than the laminar counterpart, resulting in a lower C_D than for the sub-critical case. The Reynolds numbers at which these transitions occur are sensitive to the turbulence intensity of the incoming flow and the surface roughness.

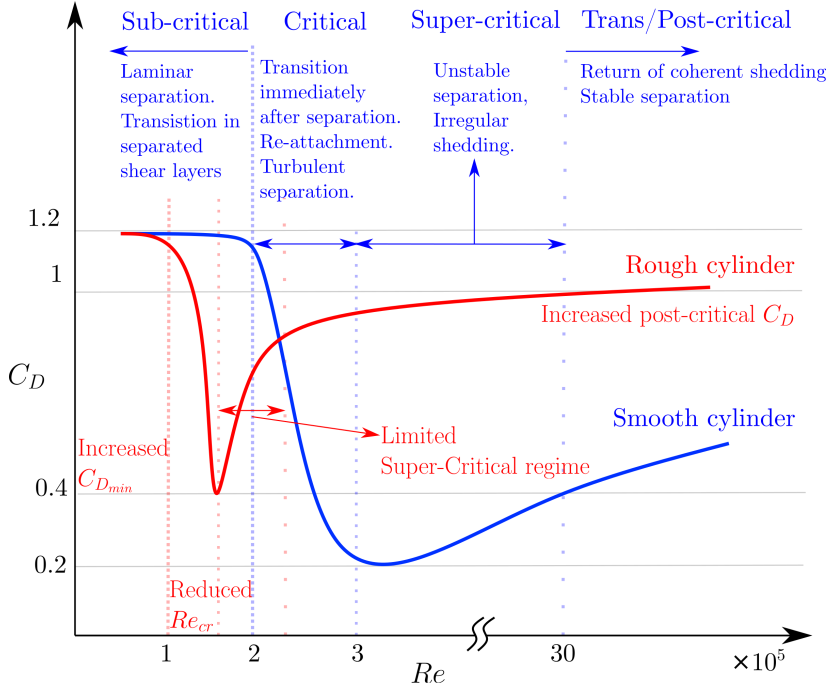Additionally, an increase in cylinder surface roughness causes (i) a decrease in

Figure 1. Schematic illustrating the four distinct high Reynolds number flow regimes over a smooth circular cylinder and the changes induced by increasing surface roughness. (Plot not to scale. Values are estimated from Schewe (1983) and the current investigation.)

the critical Reynolds number, i.e., the Reynolds number of minimum C_D, (ii) an increase in minimum C_D, and (iii) an increase in C_D in the post-critical regime. (see Fage *et al.* (1929) & Achenbach (1971)). These changes are illustrated in figure 1.

Owing to the difficulty of reaching Reynolds numbers corresponding to large engineered cylindrical structures subject to atmospheric winds (i.e. post-critical Reynolds numbers $\sim 10^7$) in wind tunnels, Szechenyi (1975) proposed the use of surface roughness to simulate post-critical flows since increasing surface roughness decreases the critical Reynolds number. Quantitatively, this is based on a curve-collapse achieved when the mean C_D and the fluctuating lift coefficient, σ_{C_L}, of cylinders of different surface roughness are plotted against a Reynolds number based on the degree of roughness ($Re_k = \rho U_\infty k/\mu$ where k denotes roughness height) – see figures 3 and 4 from Szechenyi (1975). This Reynolds number is referred to in the current work as the *Roughness Reynolds number*.

Supporting this collapse, Batham (1973) observed that mean pressure distributions on a rough cylinder at post-critical Reynolds numbers are similar to those of a smooth cylinder in turbulent incident streams at $Re \sim 10^7$. Following this, Güven *et al.* (1980) attempted to develop a theoretical framework to explain the effect of roughness on the boundary-layer development and separation points. Although they found an asymptotic post-critical C_D at large Reynolds numbers and roughness, they opined that the flow phenomena cannot sufficiently be determined through a single parameter, Re_{k_s}, and that a (joint) description

of Reynolds number and surface roughness is necessary. This conclusion was based on the large scatter in the collapse of the C_D and σ_{C_L} curves when results from different works – Achenbach (1971); Szechenyi (1975); Güven *et al.* (1980) were taken into account. Nakamura & Tomonari (1982) then posited that appropriately placed roughness strips are more effective than distributed roughness for simulating post-critical flows since the post-critical C_D of a cylinder with roughness strips is closer to that of a smooth cylinder. In contrast to the $Re(k/D)$ dependence proposed in Szechenyi (1975), a different similarity parameter, $Re(k/D)^{0.6}$, was found to result in a better collapse of the base pressure and pressure recovery obtained from cylinders of different roughness.

More recently, Eaddy (2019) measured the fluctuating lift coefficient and axial correlation length of lift for two different roughnesses and concluded that Roughness Reynolds number falls short in collapsing the fluctuating properties. While a comparison of results from different works (given in Güven *et al.* (1980)) does raise concerns about the validity of a collapse based on roughness Reynolds number, the considerable differences in blockage and aspect ratios amongst these studies weaken the significance of such a conclusion. The sensitivity of the flow to geometrical features of the setup has already been discussed in Güven *et al.* (1980), and Nakamura & Tomonari (1982), and is particularly evident in the difference in the fluctuating lift and spanwise correlation obtained from cylinders of two different aspect ratios in Eaddy (2019) (see figure 3(b)). These differences in the setups of previous studies are highlighted in the table 1.

Also evident from table 1 is the high wind-tunnel blockage ratio that has been a feature of the majority of previous works. Results were corrected for blockage effects through a technique originally proposed by Allen & Vincenti (1944), and later substantiated for cylinder flows by Farell *et al.* (1977). However, support for the assumption that blockage effects can be fully corrected comes from the collapse of only the mean drag coefficient and to a lesser extent, the surface pressure post correction. The applicability of this correction to the more sensitive fluctuating parameters, e.g. fluctuating lift, is less certain. The majority of the previous studies did not measure the fluctuating lift, and the few that did (Szechenyi (1975); Eaddy (2019)) report scatter owing to differences in geometry of the setup. Moreover, the conclusions of Eaddy (2019) and Szechenyi (1975) are inconsistent.

Fox & West (1990), with experiments on smooth cylinders at a sub-critical Reynolds number, concluded that a minimum aspect ratio of 7 is required to isolate the flow over the mid-span of the cylinder from the influence of end effects. Although their work doesn't involve rough cylinders at post-critical Reynolds numbers, it underlines the need for using high aspect-ratio cylinders with low wind-tunnel blockage. While more recent works Zan & Matsuda (e.g. 2002); van Hinsberg (e.g. 2015) incorporate such a setup, these were limited to only a single surface roughness. Thus, despite a long history, there is still a need for a more comprehensive and consistent data regarding flow over cylinders of different roughnesses at post-critical Reynolds numbers. Not only to ascertain the validity of simulating post-critical flows with larger roughness, but also to explain the influence of surface roughness on flow parameters in general.

Moreover, measurements of pressures at a single cross-section and the consequent derived coefficients of pressure drag and lift for the cylinder are incomplete without information about the extent of the spanwise correlation of the flow. As mentioned previously, in the sub-critical and the post-critical regimes, (spanwise)

organised vortex shedding is observed in cylinder wakes. Through the critical and super-critical regimes, however, this vortex shedding is less organised because of the variation of separation angle across the span caused by the high sensitivity of the LSB (Bearman 1984). This results in lower spanwise coherence through the critical regime. One measure of the spanwise correlation is the axial correlation length of the lift coefficient, Λ given by

$$\Lambda = \int_0^\infty R(s)ds \tag{1.1}$$

where R(s) is the correlation coefficient between the coefficients of lift measured at spanwise locations, $z = 0$ and $z = s$ (Norberg 2003). For smooth cylinders, the axial correlation length varies from $4-5D$ in the subcritical regime to $\sim 0.5-1.5D$ in the critical and super-critical regimes (Duarte Ribeiro 1992). Axial correlation lengths in the post-critical regime for smooth cylinders are unknown due to the difficulty in reaching high Reynolds numbers. In addition, estimates of Λ for rough cylinders are only available for a few Reynolds numbers and roughnesses. Of studies reporting on this, Ribeiro (1991) determined the correlation length for cylinder wrapped with a sandpaper roughness of $k/D = 1.8 \times 10^{-3}$ at a Reynolds number of 4×10^5 as $\sim 3.9D$, and Batham (1973) determined it to be $\sim 3.2D$ for a relative roughness of $k/D = 2.2 \times 10^{-3}$ at a Reynolds number of 2.8×10^5. Eaddy (2019) measured the axial correlation length in post-critical flows for two different roughnesses at two aspect ratios. It is of note that the higher aspect ratio (span to diameter, $AR = 9$) setup led to Λ between $2D - 3D$, while an aspect ratio of 5.7, which is closer to that of Batham (1973) ($AR = 6.6$) and Ribeiro (1991) ($AR = 6$) was found to have a larger correlation length ($\Lambda \sim 6D - 8D$). On the other hand, Buresti (1981) with hot-wire measurements in the wake, estimated the correlation length to be $\sim 4D$ in post-critical flows for rough cylinders. Information about the variation, if any, of this correlation length with roughness is limited but is required to infer the net fluctuating lift force across some length of the cylinder.

Shear-layer frequency content, f_{KH}, corresponding to Kelvin-Helmholtz waves for a smooth cylinder in the sub-critical regime is known to follow a power-law dependence based on Reynolds number, and the theoretical framework behind such a dependency was given in Prasad & Williamson (1997) (also see Thompson & Hourigan (2005)). As Reynolds number increases, the energy in the shear layer becomes more distributed and only a broad-band signature is found (Lehmkuhl *et al.* (2014)). The existence of such frequencies at post-critical Reynolds numbers and/or in the wake of rough cylinders hasn't been established, with table 1 highlighting the scarcity of wake and shear-layer measurements for rough cylinder flows.

Through the current study, we aim to provide a more comprehensive and consistent data set of lift and drag coefficients, surface pressure distributions, and spanwise correlation lengths, providing the variation of these properties with roughness and Reynolds number in post-critical flows. This data tests the validity of whether flow parameters collapse based on Roughness Reynolds number alone. With the help of various measurement techniques, we aim to explore similarities and differences between the wakes from cylinders of different surface roughnesses at the same post-critical Reynolds number, and also at the same Roughness Reynolds number. This exploration augments our understanding of the influence of surface roughness on the flow over and forces on circular cylinders, enabling the prediction of aerodynamic loads at Reynolds numbers often relevant to large

Experiment	Data	Aspect ratio	Blockage	Relative Roughness $k/D \times 10^3$
Achenbach (1971)	P, τ	3.3	16.67%	1.1, 4.5, 9 [+]
Batham (1973)	P, C	6.6	5%	2.2
Szechenyi (1975)	P	4–9.3	7–23%	0.15-2
Güven *et al.* (1980)	P, B	3.08	17.8%	2.5–6.2[+]
Buresti (1981)	P, C	6.6–23	3-10%	0.91–12.35
Nakamura & Tomonari (1982)	P	3.3	15.5%	0.9–10
Ribeiro (1991)	P, C	6	12%	1.8
Chakroun *et al.* (1997)	P	5.98	16.6%	1.1–2.3
Zan & Matsuda (2002)	F	10	2.5%*	0.1
Eaddy (2019)	P, C	5.7,9	12%, 8%	0.74,2.48,4.22
van Hinsberg (2015)	P, F	10	10%	1.2[+]
Current	P, C, W	9.8	5%	1.1-3[+]

Table 1. A non-exhaustive list of previous investigations concerning rough cylinders and the measurement techniques used. P: C_D, C_L obtained from integration of pressure distribution, F: C_D, C_L obtained from total force measurements, τ: Skin-friction measurements, B: Boundary-layer measurements, W: Wake measurements C: Spanwise correlations. *: Porous walls and a suction plenum were also used to reduce blockage effects. [+]: Values given are the equivalent sand grain roughness measures. (Nikurdase (1933)).

engineered structures. Additionally, information about wake width and wake frequencies helps in understanding and predicting the aerodynamics of multiple cylindrical structures in close proximity.

For the remainder of this paper, further discussion is split into three sections. §2 gives the geometric details of the setup and describes the data acquisition and post-processing. Results are discussed in §3, and §4 summarises the key conclusions from the current work.

2. Methodology

2.1. *Experimental setup*

Experiments were conducted in a closed circuit wind tunnel with a 2000 mm tall and 4000 mm wide rectangular cross-section. The turbulence intensity of the incoming flow is 1.35% at the centre of the cylinder, which is positioned 4600 mm downstream from the start of the working section. At 35 m s^{-1} (corresponding to a Reynolds number of $\sim 4.5 \times 10^5$ based on cylinder diameter), displacement thickness and momentum thickness of the vertical boundary layers are ~ 12 mm and ~ 10 mm, respectively, near both the floor and the roof of the test section at the point where cylinder is installed. Outside the boundary layers, variation in the local mean velocity is within 0.5% of the global mean measured along the axis of the cylinder.

The diameter of the cylinder, D, is 204 mm including the thickness of the sandpaper backing cloth and the average roughness height. It spans the height of the tunnel (2000 mm), thereby resulting in an aspect ratio of ~ 9.8 and blockage ratio of $\sim 5\%$. It consists of two separate spanwise sections to facilitate the installation of pressure taps. The lower section is made of steel to lend overall strength, while the section with pressure taps is made of aluminium. To increase the uniformity in diameter, the steel section is formed by turning a cylinder

Sandpaper grade	P40	P60	P80	P100
Average grain size, k (microns)	412	262	196	157
Relative roughness, $k/D \times 10^3$	2.01	1.28	0.96	0.76
Equivalent sand grain roughness, $k_s/D \times 10^3$	3	1.9	1.4	1.1

Table 2. Different grades of sandpaper used and the corresponding roughness measures.

of larger diameter while machined bulkheads are inserted inside the aluminium section at regular intervals. The resulting variation in the diameter of the cylinder over the entire span is $< 1\%$. These two sections are joined from inside in order to reduce the degree of non-uniformity on the outer surface. The seam due to the joint between these two sections is ~ 0.5 mm and $1.4D$ away from the nearest measurement plane, and hence is expected to have negligible influence on the measurements. The cylinder is also fixed at the roof of the tunnel to further reduce the vibrations and the influence of any gap flow.

The desired uniform surface roughness is achieved by wrapping sandpaper around the bare cylinder. The spanwise seam from joining the two ends of the sandpaper is at $180°$ (i.e. in the wake region). The types of sandpaper used, and the corresponding average roughness heights,k are given in table 2.

Equivalent sand grain roughness, k_s, is the uniform sand grain height that generates a similar frictional velocity deficit in a fully rough flow determined from Nikurdase (1933). Achenbach & Heinecke (1981) conducted experiments to determine values of k_s of 4.5×10^{-3} and 1.1×10^{-3} for 40 grit and 120 grit sandpapers thereby yielding k_s/k of 1.57 and 1.43, respectively. A similar average conversion factor of $k_s/k \sim 1.5$ for sandpaper grits was found in Speidel (1954). In the absence of experiments to determine the exact value of k_s for the sandpapers used in the current work, the conversion factor $k_s/k = 1.5$ is used for all of the grits examined to ascertain the equivalent sand grain roughness.

Four cross-sections along the span are chosen for pressure measurements, located at heights of $0D$, $-1D$, $1D$, and $2D$, where $0D$ is for the spanwise mid-plane of the cylinder and the axis is positive towards the roof. Each of these cross-sections consists of 30 uniformly distributed pressure measurement locations that were installed after wrapping the sandpaper onto the surface. These locations contain a 20 mm long hypodermic tube of 2 mm outer diameter and 1.5mm inner diameter, which is attached from inside of the cylinder and positioned carefully to end at the backing cloth of the sandpaper so not to protrude above the trough of the roughness elements. Flexible PVC tubes of length 2200 mm were then used to connect these hypodermic tubes to the pressure measurement system. Cross-sectional measurement planes, the joint between the sections, and the pressure ports are illustrated in figure 2.

2.2. *Data acquisition and post-processing*

Pressure at the above-mentioned locations was sampled at 2000 Hz for at least 120 s using a TFI synchronous Differential Pressure Measurement System. An amplitude and phase correction was applied to the instantaneous pressure data to account for the length and diameter of pressure tubing. The recorded pressure data was transformed into the frequency domain and a transfer function was applied before transforming the data back into the time domain. This transfer
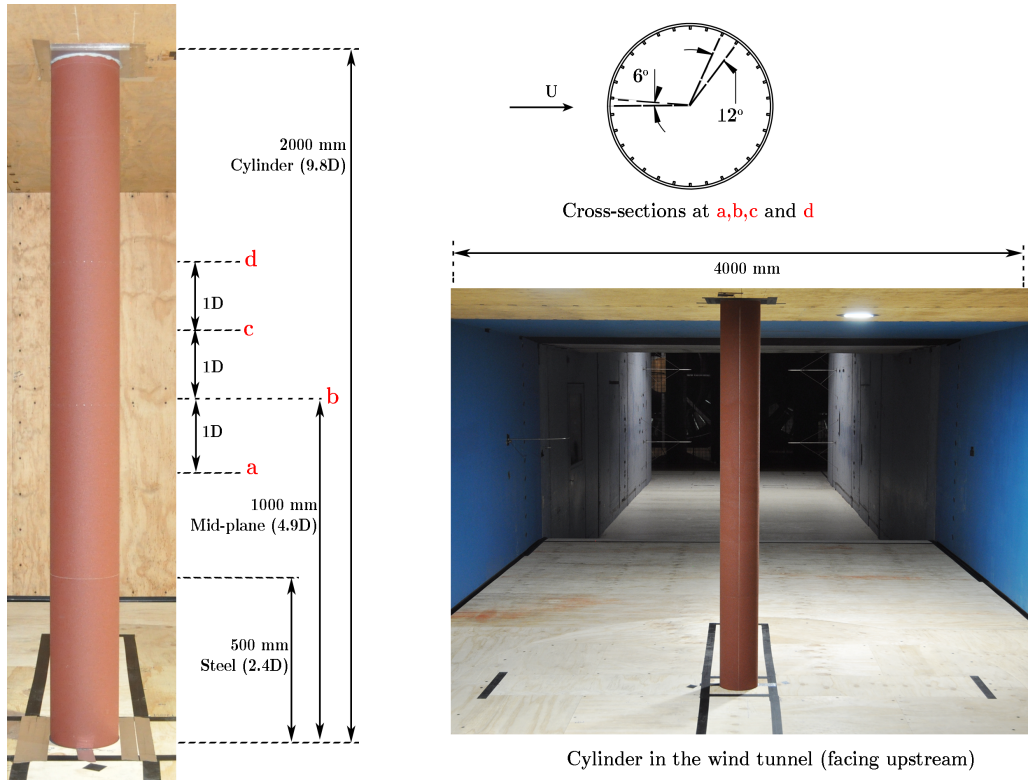
Figure 2. Schematic of the setup showing a cylinder with sandpaper attached, its dimensions and measurement planes on the left, pressure tap locations at the top right, and placement of the cylinder in the working section of the tunnel at the lower right.

function was computed based on the length and the diameter of the pressure tube following the procedure given in Bergh & Tijdeman (1965) and is reported in the figure 18 in the appendix. The amplitude response of the theoretical transfer function falls below 0.4 at ~ 500 Hz and below 0.25 at $f \sim 630$ Hz. The pressure signals were cut off at ~ 630 Hz and spectra from these signals reported in this investigation were only plotted till 250 Hz.. The test duration amounts to more than 600 shedding cycles at the lowest Reynolds number presented here and more than 2000 shedding cycles at post-critical Reynolds numbers, which form the crux of the discussion. Sectional mean and fluctuating pressures presented here were obtained from tests of longer duration (~ 5000 shedding cycles) and these tests were also used to establish the convergence of C_D and σ_{C_L} for the shorter tests.

Flow parameters at each Reynolds number were measured at least three times and the data reported includes 90% confidence intervals based on t-distribution statistics. Confidence intervals (CI) for a parameter is computed using

$$CI(x) = t(n-1)_{\alpha/2} \times \frac{\sigma_x}{\sqrt{n}}. \tag{2.1}$$

where $t(n-1)_{\alpha/2}$ is the critical t-value for a significance level of α and $n-1$ degrees of freedom. Here, n is the number of tests, x is the parameter of interest and σ_x is the standard deviation of the parameter across the repeat tests. For the current investigation α is chosen to be 0.10, thus yielding a two-sided 90% confidence

interval. Thus, if the same tests and processing were to repeat a number of times, the confidence intervals present the bounds inside which the sample mean lies 90% of the time.

Instantaneous coefficients of pressure drag and lift were obtained by integrating the circumferential pressure distributions and the corresponding mean and standard deviations were then obtained from these instantaneous coefficients. All the data presented here is the mean of the four spanwise measurement planes except in figure 8 for which instantaneous pressure distributions from the mid-plane are presented. Within the post-critical regime, variation in the coefficient of drag measured from different cross-sections was within 2% of the spanwise mean for all roughnesses tested and this variation reduced with decreasing roughness.

In an attempt to reduce the error in estimates of the drag coefficient, C_D, the minimum pressure coefficient, C_{P_m}, and the base pressure coefficient, C_{P_b}, due to linear interpolation of the discrete pressure distribution, the mean pressure distribution along each cross-section was interpolated using *Modified Akima Interpolation* (Akima (1970)) before obtaining these parameters. This method was chosen over the traditional linear, cubic or spline interpolation since it minimises potential overshoots near the separation region. The effectiveness of this interpolation method was tested using continuous distributions obtained from CFD and also from finer surface pressure measurements from the literature (Achenbach (1971); Cheung & Melbourne (1995); Güven *et al.* (1980); van Hinsberg (2015); Ribeiro (1991)). Amongst the different circumferential pressure distribution profiles tested, the maximum deviation in estimates between the interpolated C_D, C_{P_m} and continuous C_D, C_{P_m} are 0.8% and 2%, respectively, while the difference between the linear C_D, C_{P_m} and continuous C_D, C_{P_m} estimates are 1% and 4% respectively.

A TSI 1201 platinum hot film was used with a 1750 constant temperature anemometer to measure the instantaneous planar velocity magnitude and hence estimate the predominantly streamwise velocity distribution in the immediate wake. This allowed a quantification of the shear layer thickness and frequency content in the separating shear layers. A 50μ wide, 1mm long single-axis film with its axis parallel to the axis of the cylinder was mounted on a traverse system for this purpose. Velocity calibrations were performed to obtain a fifth order polynomial to convert from voltage measurements of the film to the flow velocity. The upper frequency limit, $f_c(-3 \text{ dB})$ for this arrangement is determined through a 1 kHz square wave input as 12.5 kHz (based on Freymuth (1977); Brunn (1995)). Data from this hot film was acquired at 50 kHz for a period of at least 60 seconds (~ 1200 shedding cycles at the lowest speed of measurement). Spectra for the separated shear layer were obtained through velocity time series lasting 240 seconds (figure 17) and are plotted only to 6 kHz and the shear layer frequencies discussed were < 300 Hz, well below f_c.

The blockage ratio of the setup was only 5% and hence, the influence of the closeness of wind-tunnel walls is expected to be small. Nevertheless, mean values of C_D, C_P, and Re are corrected for blockage according to the procedure described in Roshko (1961) (based on Allen & Vincenti (1944)) in order to provide easier comparison with the literature. (The accuracy of the blockage correction for the mean coefficients of drag and pressure has been previously verified by Farell *et al.* (1977).) The fluctuating properties such as σ_{C_P} and σ_{C_L} have not been corrected for blockage since the applicability of blockage corrections to these parameters
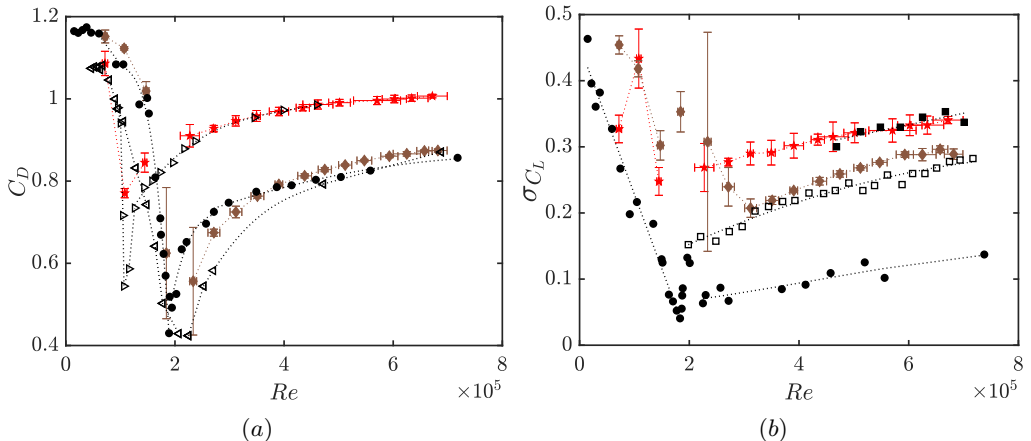
Figure 3. A comparison of (a) the mean drag coefficient, and (b) the fluctuating lift coefficient in this study with earlier works. Confidence intervals were calculated as described in §2.2 ··◁·· Achenbach (1971), $k_s/D = 1.1 \times 10^{-3}$; ··●·· van Hinsberg (2015), $k_s/D = 1.2 \times 10^{-3}$; ··▷·· Güven *et al.* (1980), $k_s/D = 3.11 \times 10^{-3}$; ··□·· Eaddy (2019), $k_s/D = 1.2 \times 10^{-3}$, $k/D = 0.8 \times 10^{-3}$, AR: 9. ··■·· Eaddy (2019), $k_s/D = 1.2 \times 10^{-3}$, $k/D = 0.8 \times 10^{-3}$, AR: 5.7; ··◆·· Current, $k_s/D = 1.1 \times 10^{-3}$; ··★·· Current, $k_s/D = 3 \times 10^{-3}$.

hasn't yet been established and the corrections are likely small. The maximum difference between the raw and the blockage corrected coefficients of drag is 3%.

3. Results and discussion

3.1. *Drag and lift coefficients*

Figure 3 plots, for a number of studies, the relationship of both the mean drag coefficient, C_D, and the fluctuating lift coefficient, σ_{C_L}, with Reynolds number. For clarity, the results of only the smoothest and the roughest cylinder in the current study are given in this figure. Figure 3(a) includes C_D measurements from the sectional pressure measurements of van Hinsberg (2015) while those obtained from their force measurements are excluded. Within the post-critical regime, the degree of agreement in C_D amongst the works is high, and perhaps surprising given the differences in the aspect and blockage ratios of their set-ups (see table 1). A reduction in aspect ratio is expected to decrease drag since the fluid feeding from the edge of the cylinder increases the base pressure (Basu (1985)). Considering the large difference in the blockage ratios amongst the different setups (from 5% to 18%); this agreement is indicative that blockage corrections work well for the predictions of C_D.

Figure 3(b) gives the variation of the fluctuating coefficient of lift with Reynolds number. The scatter in measurements of σ_{C_L} across different investigations is comparatively larger than that of C_D owing to its higher sensitivity to aspect ratio, blockage ratio, mode of generation of roughness and method of measurement (Norberg (2003)). In particular, the influence of aspect ratio and blockage is also evident in the difference in σ_{C_L} obtained from two different setups of the same roughness in Eaddy (2019). While their larger aspect ratio ($AR = 9$) results for similar roughness agree well with the current study, σ_{C_L} values from the smaller aspect ratio ($AR = 5.7$) are considerably higher.

On the other hand, σ_{C_L} reported in van Hinsberg (2015) is much lower than

that for the current study at the same Reynolds number (~ 0.1 compared to ~ 0.25) despite both setups having similar aspect ratio and relative roughness. A possible cause of this discrepancy is the method of generating and representing roughness. While van Hinsberg (2015) used plasmatic metal coating to generate surface roughness, the current work uses sandpaper. The roughness of a sandpaper is expected to be more randomly distributed than that obtained from machining the surface. The agreement in the mean C_D indicates that the influence of the roughness on the broad flow features is similar in the two investigations. The relatively large disagreement in σ_{C_L} could, in part, be due to the distribution of roughness and the resulting variation across different methods of generation.

In addition to the mode of roughness generation, the technique used for determining σ_{C_L} in the two studies is also different. van Hinsberg (2015) measured the instantaneous forces on the entire cylinder using a force balance to determine the fluctuating lift coefficient. In contrast, for the current study, the time-varying lift coefficient and its standard deviation are obtained through the integration of instantaneous pressure coefficients at a single cross-section of the cylinder. This suggests that the spanwise correlation of fluctuating force components plays an important role; this will be examined in more detail in §3.5. Moreover, preliminary experiments during the initial phase of the current study revealed high sensitivity of σ_{C_L} to the presence of a gap between the cylinder and wind-tunnel walls that is required in order to measure forces through piezo-electric balances. Kacker *et al.* (1974) reported that an airgap between the active and dummy cylinder as small as 0.1 mm could result in lift force measurements 5 to 10 times smaller than the actual value. Jones *et al.* (1969) also found that gaps of 0.7 mm could have significant effects on the flow configuration over a smooth cylinder. More information about the influence of this gap and differences between lift coefficients measured through total force and cross-sectional pressure methods for smooth cylinders is given in Norberg (2003).

Limited and widely varying data amongst different studies and increased sensitivity of the lift to the parameters of flow setup makes comparisons of σ_{C_L} for rough cylinders particularly difficult. Scarcity of information about σ_{C_L} for different roughnesses in the post-critical regime was a major motivation behind this work and the results presented here aim to address this knowledge gap.

Figure 4 gives the variation of the mean coefficient of drag and the fluctuating lift coefficient with Reynolds number for different roughnesses. Flow parameters in the critical/super-critical regime where the cylinder flow experiences combinations of *laminar separation, transition to turbulence in the shear layer, turbulent reattachment, intermittent turbulent separation, and asymmetric shedding* are very sensitive to disturbances in the flow and hence, the confidence intervals are larger. This region of high sensitivity extends up to $Re \sim 2.3 \times 10^5$ for the smoothest roughness tested and up to $Re \sim 1 \times 10^5$ for the roughest tested in the current work. Owing to the higher sensitivity of the lift to the pressure distribution near separation, these confidence intervals for the measurements of σ_{C_L} are larger than those of C_D. Tests for the same roughness and similar Re are found to intermittently contain the LSB for different proportions of time resulting in a wide range of σ_{C_L}, thus making it difficult to infer representative trends through the critical regime. The reader is referred to Cadot *et al.* (2015) for more information regarding the flow configuration and the stability of LSB through the critical regime. Note that § 3.4 explores the intermittency of the LSB and the influence of roughness in further detail. Repeatability is improved
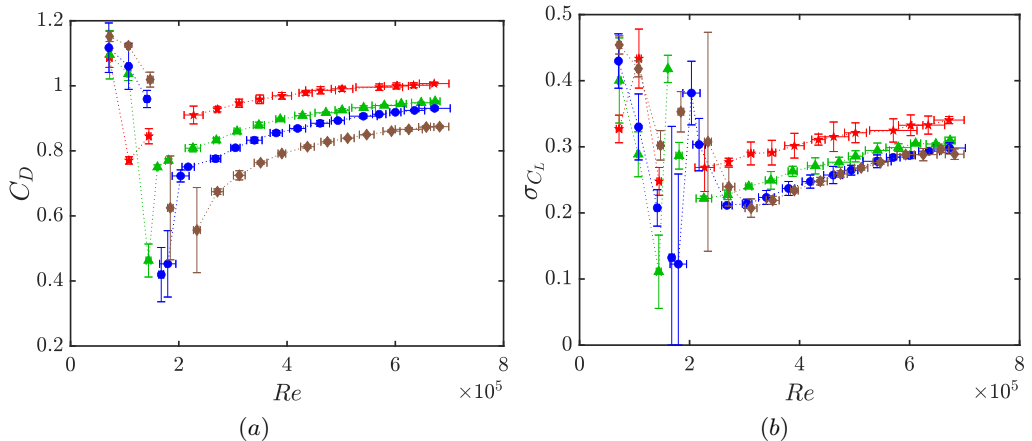
Figure 4. (*a*) Mean coefficient of drag, C_D, and (*b*) fluctuating coefficient of lift, σ_{C_L} for different roughness. Confidence intervals were calculated as described in §2.2 ··⋆··: $k_s/D = 3 \times 10^{-3}$, ··▲··: $k_s/D = 1.9 \times 10^{-3}$, ··●··: $k_s/D = 1.4 \times 10^{-3}$, and ··◆··: $k_s/D = 1.1 \times 10^{-3}$.

beyond the critical regime and the observed variations with Reynolds number are relatively smooth.

An increase in roughness leads to a reduction in the critical Reynolds number, the Reynolds number at which C_D is minimum. Roughness particles promote the transition to turbulence near the surface of the cylinder and hence, an increase in roughness leads to an earlier transition in the boundary layer, i.e. transition to turbulence immediately after separation, and the LSB occurs at a lower Reynolds number for larger roughness. From the current tests, the critical Reynolds number of the roughest surface tested ($k_s/D = 3 \times 10^{-3}$) is $\sim 1 \times 10^5$ while that of the smoothest surface tested ($k_s/D = 1.1 \times 10^{-3}$) is $\sim 2 \times 10^5$. Beyond the critical Reynolds number, the flow configuration changes from stable reattachment of the separation bubble on both sides of the cylinder to asymmetric reattachment and eventually to no reattachment on the two sides of the cylinder (Cadot *et al.* 2015). This results in an increase in C_D increase as Reynolds number increases in the super-critical regime. Increasing roughness causes the LSB to become more unstable, thereby leading to a lower range of Re where an intermittent LSB occurs and hence, a smaller super-critical regime. By destabilising the LSB, roughness promotes coherent vortex shedding over the span of the cylinder and hence increases the forces on the overall span of the cylinder since the flow separates earlier when the LSB is absent.

At post-critical Reynolds numbers, the boundary layer in the adverse pressure gradient region is turbulent and hence, separates later than the laminar boundary layer of sub-critical regime. Due to this delayed separation, the post-critical C_D is lower than that of the sub-critical C_D for a given roughness. On the other hand, an increase in surface roughness causes an earlier separation of turbulent boundary layers in adverse pressure gradients due to an increased momentum deficit near the wall (Song & Eaton (2002); Aubertine *et al.* (2004)). Thus, at a fixed post-critical Re, C_D increases with an increase in roughness. The mean coefficients of drag C_D are found to be ~ 0.87 and ~ 1.01, respectively, for the smoothest and roughest cylinders at the highest Reynolds number of the current tests (6.8×10^5).

Similar to C_D, the post-critical σ_{C_L} increases with increasing roughness. Power spectra of the velocity fluctuations given in figure 16 reveal an increased energy content at the shedding frequency for increased roughness. This indicates that an increase in roughness results in larger fluctuations and hence a larger σ_{C_L}. At $Re \sim 6.7 \times 10^5$, σ_{C_L} is 0.28 and 0.34, respectively, for the smoothest and roughest cylinder tested.

3.2. *Circumferential pressure distributions*

Mean and standard deviation circumferential pressure distributions presented in this study are the average of distributions over the four spanwise locations. To better highlight variations, these spanwise averages are presented only for half of each circumference. These half-circumference pressure distributions are the average of the upper and lower halves of the cylinder. Across all the post-critical Reynolds numbers ($Re \geqslant 3 \times 10^5$) and roughnesses tested, the maximum deviation, $|\overline{C_P}(\theta) - \overline{C_P}(360 - \theta)|$ is 0.1 and this is seen in the large gradient region of $0° \leqslant \theta \leqslant 90°$. Over $100° \leqslant \theta \leqslant 180°$, this maximum reduces to < 0.01. The mean deviation across all the tests is less than 0.08 for $0° \leqslant \theta \leqslant 180$.

Figure 5 gives the circumferential mean pressure coefficient of cylinders of different roughnesses at post-critical Reynolds numbers. For a given roughness, the coefficient of pressure over the upstream region of the cylinder ($\sim (300°\text{--}0°\text{--}60°)$) doesn't exhibit any noticeable change with Reynolds number, generally following the potential flow solution. The observable changes with increasing Reynolds number are a decrease in the coefficient of pressure in the downstream/base region ($\sim (100°\text{--}180°\text{--}260°)$), and an increase in the coefficient of pressure in the acceleration region ($\sim (75°\text{--}90°)$).

To examine these changes in further detail, three additional variables are introduced. Base pressure, C_{P_b}, is the mean coefficient of pressure over the downstream side of the cylinder. Minimum pressure, C_{P_m}, is the minimum coefficient of pressure on the cross-sectional surface. Wake angle, θ_w, is the angle at which a linear regression fit of the coefficient of pressure profile from C_{P_m} to C_{P_b} intersects C_{P_b}. Both C_{P_m} and θ_w given are the mean of the values found on each half of the cylinder. Furthermore, all three variables presented are the corresponding spanwise averages over a sample of four cross-sections. The definitions of these variables for a representative C_P distribution are given in the figure 6(*a*).

While C_{P_b} forms the prominent contribution to the coefficient of drag, C_{P_m} is indicative of the degree of deceleration of flow velocity near the surface of the cylinder, i.e., the lower the C_{P_m} the higher the velocity outside the boundary layer. Also, θ_w is a nominal estimate of the separation angle obtained from the circumferential mean C_P distribution. This estimate is smaller than the actual separation angle given by θ_s by $\sim 5°$ (Güven *et al.* (1980)); indeed this correlates well with the θ_s measurements of Achenbach (1971) as seen in figure 6(*b*).

On the surface of a smooth cylinder, the laminar boundary layer in the sub-critical flow separates earliest, near $\sim 80°$ on a smooth cylinder, followed by a turbulent boundary layer, between $\sim 100 - 110°$ on a smooth cylinder, and a boundary layer with a laminar separation bubble in the critical regime separates more downstream, between $\sim 120° - 140°$ on a smooth cylinder than the latter (Basu (1985)). A similar trend is observed in the measurements of θ_w against Reynolds number from the current results. At sub-critical Reynolds numbers, θ_w is $\sim 75°$ for all the roughnesses tested and an increase in Reynolds number
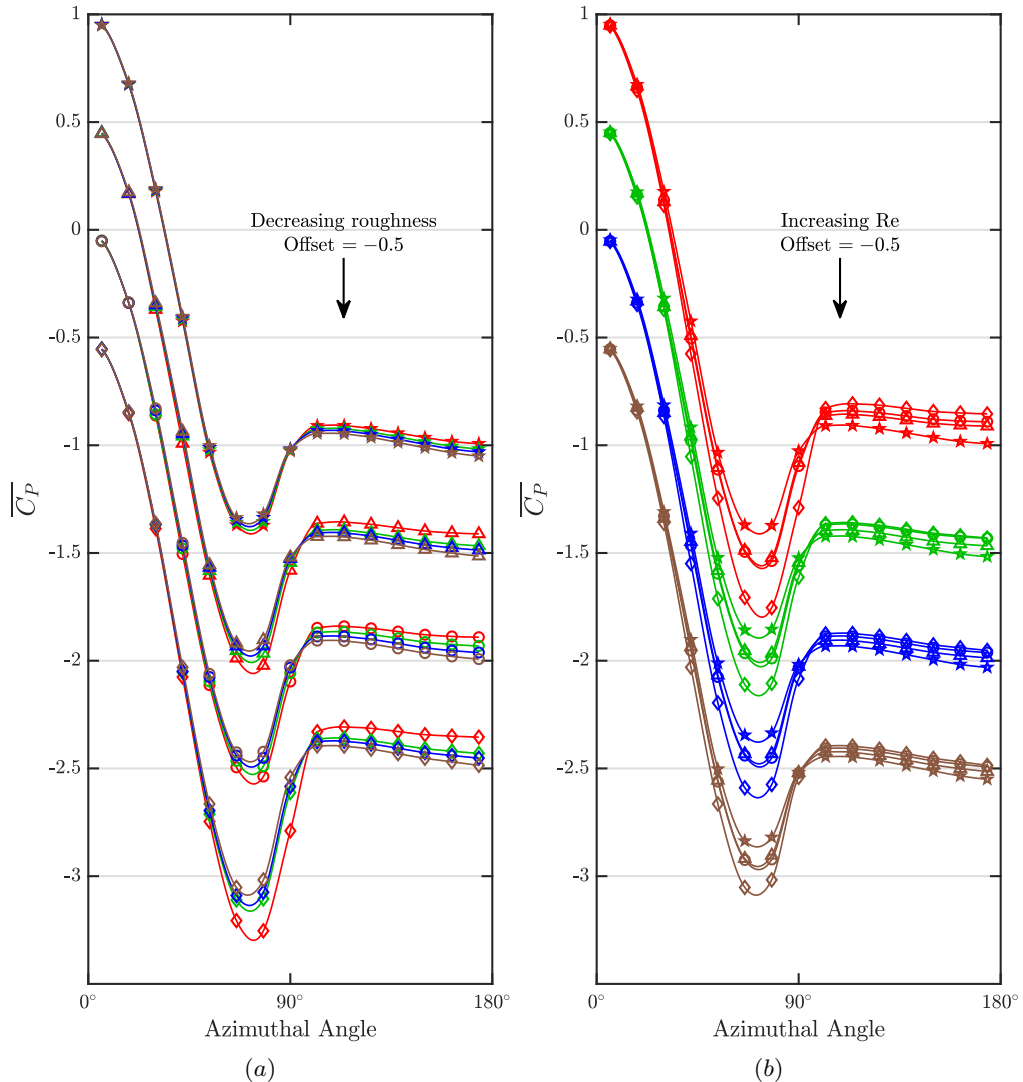
Figure 5. Circumferential distributions of mean coefficient of pressure. $\star$: $k_s/D = 3 \times 10^{-3}$, $\triangle$: $k_s/D = 1.9 \times 10^{-3}$, $\bigcirc$: $k_s/D = 1.4 \times 10^{-3}$ and $\Diamond$: $k_s/D = 1.1 \times 10^{-3}$. ——: $Re \sim 3 \times 10^5$, ——: $Re \sim 4 \times 10^5$, ——: $Re \sim 5 \times 10^5$, and ——: $Re \sim 6.7 \times 10^5$. (*a*) Effect of Reynolds number for different roughness. (*b*) Effect of roughness for different Reynolds number. Note that successive families of curves have been offset in the pressure coefficient by -0.5.

results in an increasing θ_w until it reaches a maximum ($\sim 108°$ and $\sim 125°$ for the roughest and the smoothest cylinder, respectively). A further increase leads to a decrease in the wake angle and at large post-critical Reynolds numbers the wake angle approaches an asymptotic value of $\sim 95°$. This indicates that the separation angle also reaches an asymptotic value of $\sim 100°$ in agreement with Achenbach (1971).

Similar to the wake angle, the base pressure coefficient increases and then decreases with increasing Reynolds number. The peak in the base pressure occurs in the critical regime and coincides with the peak in the separation angle and also the minimum drag coefficient. As the Reynolds number is increased further, the

change in base pressure decreases until eventually approaching an asymptotic value of ~ -0.95. The convergence of C_{P_b} with roughness at large Reynolds numbers is slightly wider than that of θ_w. Changes in the minimum pressure, C_{P_m} are in the opposite direction, i.e. an increase in Reynolds number causes a decrease and then an increase in C_{P_m}, before eventually approaching an asymptotic value. Unlike θ_w and C_{P_b}, the asymptotic value in the minimum pressure at the highest Reynolds numbers tested is a function of roughness, with larger roughness leading to a higher C_{P_m}, i.e. larger deceleration of the flow.

For the smoothest cylinder tested ($k_s/D = 1.1 \times 10^{-3}$), the changes in θ_w, C_{P_b} and C_{P_m} when the Reynolds number is increased from $Re \sim 4 \times 10^5$ to $Re \sim 6 \times 10^5$ are approximately 4%, 6% and 5%, respectively. The corresponding changes for the roughest cylinder tested ($k_s/D = 3 \times 10^{-3}$) are 1%, 3% and 2%, respectively. At the largest Reynolds number tested ($Re \sim 6 \times 10^5$), the changes in these quantities from the smoothest cylinder to the roughest cylinder tested are 3%, 5% and 14%, respectively. These observations indicate that while the flow near and beyond separation becomes nearly independent of roughness at large Reynolds numbers, flow in the deceleration region and particularly near the minimum pressure is still dependent on the degree of surface roughness, even though it is relatively independent of the Reynolds number.

Amongst different investigations, the degree of scatter in the pressure rise to separation $C_{P_b} - C_{P_m}$ is slightly larger than that in C_D and C_{P_b} (note the different y-scales in figures 6(c) and 6(e)). This is contrary to the proposal of Güven *et al.* (1980) and Farell *et al.* (1977) that the pressure rise to separation is less sensitive to the effects of aspect ratio and blockage than C_{P_b} and C_{P_m}. The present rough cylinder data shows that the base pressure results among different studies have a smaller scatter followed by the minimum pressure. The deviation in the pressure rise to separation is a consequence of that in minimum pressure. In this regard, the use of spanwise variation of minimum pressure to ascertain the effects of blockage and aspect ratio in the post-critical region is recommended over the base pressure distribution that has been used before (Fox & West (1990); Stansby (1974)).

Blockage corrections to pressure distributions (Allen & Vincenti (1944); Roshko (1961)) don't include the effect of wake blockage on pressure gradients (Farell *et al.* (1977)) and is a possible cause of the larger scatter in the pressure distribution parameters from different studies when compared to that of C_D. Another limitation in the application of blockage corrections is that the corrected C_P distributions don't directly correspond to the corrected C_D values since the corrections are independent. In this context, one should exercise care in applying the corrections to predict the pressure distributions free of wind-tunnel influences, since an agreement in the blockage corrected C_D doesn't imply agreement in the blockage corrected C_P. Moreover, corrections to σ_{C_L} are unavailable since the influence of blockage on the fluctuating parameters is still uncertain. This emphasises the importance of data obtained from a high aspect ratio and low blockage setup similar to the one used in the current work.

Since wake angle and base pressure appear to be in good correlation, the coefficient of base pressure, C_{P_b}, is plotted against the wake angle θ_w in the post-critical regime ($Re \geqslant 3 \times 10^5$) in figure 6(f). The data plotted is obtained from tests of different roughnesses i.e. different minimum pressure (see figure 6(c)) and thus, a different pressure distribution before separation. Hence, a good correlation across different roughnesses indicates that the base pressure is a strong function of the separation angle and only a weak function of the flow before separation
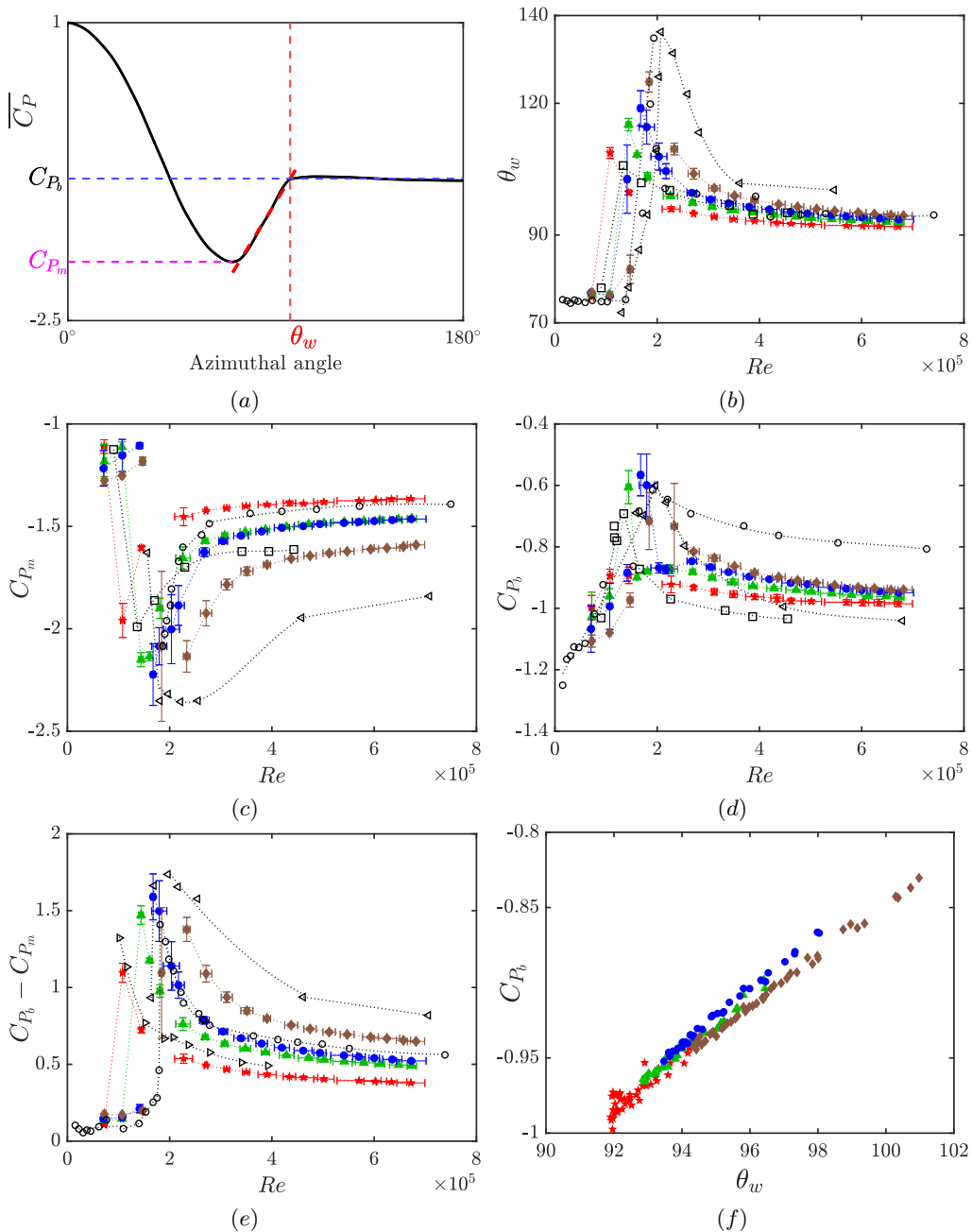
Figure 6. (a) Parameters of coefficient of pressure, Variation of (b) Wake angle, (c) Coefficient of minimum pressure and (d) Coefficient of base pressure. (e) Pressure rise to separation with Reynolds number and (f) Base pressure vs Separation angle. Confidence intervals were calculated as described in §2.2 Current: $\cdots\star\cdots$ $k_s/D = 3 \times 10^{-3}$; $\cdots\blacktriangle\cdots$ $k_s/D = 1.9 \times 10^{-3}$, $\cdots\bullet\cdots$ $k_s/D = 1.4 \times 10^{-3}$; $\cdots\blacklozenge\cdots$ $k_s/D = 1.1 \times 10^{-3}$; $\cdots\bigcirc\cdots$ van Hinsberg (2015) $k_s/D = 1.2 \times 10^{-3}$; $\cdots\triangleleft\cdots$ Achenbach (1971), $k_s/D = 1.1 \times 10^{-3}$; $\cdots\triangleright\cdots$ Güven *et al.* (1980), $k_s/D = 3.11 \times 10^{-3}$, $\cdots\square\cdots$ Güven *et al.* (1980), $k_s/D = 2.5 \times 10^{-3}$.

in the post-critical regime. From figure 6(b), in post-critical flows, an increase in roughness at a constant Reynolds number or an increase in Reynolds number for a fixed roughness lead to a decrease in the separation angle. Figure 6(f) indicates that the change in base pressure coefficient arising due to a change in the separation angle is similar for all roughnesses tested. Since the base pressure coefficient forms the major contribution to the coefficient of drag, this results in the drag coefficient being similar in post-critical flows regardless of whether the separation angle is a result of increasing roughness or increasing Reynolds number. This forms the basis for collapse of C_D when plotted against Roughness Reynolds number, Re_{k_s}, and this is further discussed in § 3.7.

3.3. *Fluctuating pressure coefficient*

Figure 7 gives the distribution of the fluctuating pressure coefficient on the cylinder surface at different Reynolds numbers and roughnesses. The two significant trends with increasing Reynolds number post the critical regime are an increase in σ_{C_P} over the circumference (more evident in the downstream region); and an upstream movement of the angle at which σ_{C_P} is maximum. A peak in σ_{C_P} is an indication of boundary-layer separation in the vicinity and since separation moves upstream with increasing Reynolds number, the location of maximum σ_{C_P} also moves upstream. The smaller local maximum near $\sim 160°$ might indicate shear-layer roll up closer to the surface of the cylinder near that region. This smaller peak is less significant at lower Reynolds numbers (near $Re \sim 3 \times 10^5$) especially for the smoother cylinders due to weaker vortex shedding at those Reynolds numbers. For a given roughness, an increase in velocity leads to an increase in the turbulent kinetic energy near the surface, causing an overall increase of σ_{C_P} as the Reynolds number is increased. Moreover, earlier separation is also expected to cause larger fluctuations in the downstream region of the cylinder.

Figure 7(b) gives the variation of σ_{C_P} with roughness for various Reynolds numbers. For a given Reynolds number, σ_{C_P} increases over the circumference of the cylinder with an increase in roughness. In addition, the peak in σ_{C_P} increases and moves upstream as roughness is increased for a fixed Reynolds number. This change is similar to that seen when Reynolds number is increased for a fixed roughness.

3.4. *Power spectra of lift and Strouhal number of vortex shedding*

Figure 8(a) gives the Power Spectral Density (PSD) of fluctuations in the lift coefficient at a Reynolds number of 6.7×10^5 for different roughnesses. A similar distribution with a significant peak is seen in the majority of the tests (all at post-critical Reynolds numbers) indicating the presence of strong periodic vortex shedding. Since the lift force is induced by the alternating vortex shedding, the second half of the lift cycle must mirror the first half, which means only odd harmonics can contribute to a periodic signal. This can be seen in the presence of the third harmonic throughout the post-critical regime.

Achenbach & Heinecke (1981) found that energy of lift fluctuations is distributed in a narrow band of frequencies for rough cylinders through the critical regime, while on the other hand Szechenyi (1975) and Batham (1973) found a broadband spectra without an obvious dominant frequency near the critical Reynolds number. A clear shedding frequency was found in the lift spectra for all tests except for $k_s/D = 1.4 \times 10^{-3}$ and $k_s/D = 1.1 \times 10^{-3}$ at Reynolds numbers
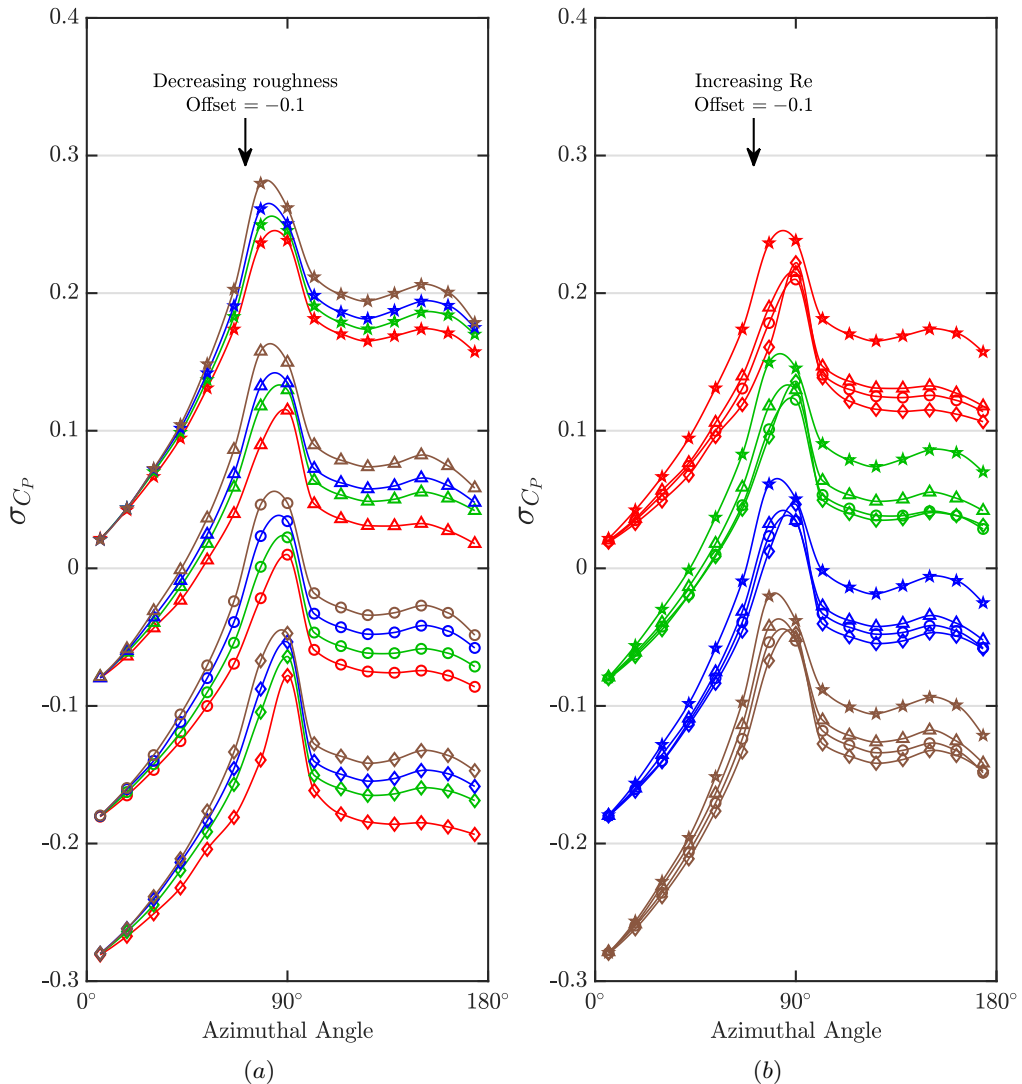
Figure 7. Circumferential distributions of the fluctuating coefficient of pressure. $\star$: $k_s/D = 3 \times 10^{-3}$, $\triangle$: $k_s/D = 1.9 \times 10^{-3}$, $\bigcirc$: $k_s/D = 1.4 \times 10^{-3}$ and $\lozenge$: $k_s/D = 1.1 \times 10^{-3}$. ——: $\sim 3 \times 10^{5}$, ——: $\sim 4 \times 10^{5}$, ——: $\sim 5 \times 10^{5}$, and ——: $\sim 6.7 \times 10^{5}$. (*a*) Effect of Reynolds number for different roughness. (*b*) Effect of roughness for different Reynolds number. Note that successive sequences of curves have been offset in pressure coefficient by -0.1.

near $Re \sim 2 \times 10^{5}$. As an example, gives time histories of the coefficients of pressure, lift and drag (plotted against a non-dimensional convective time scale, tU_∞/D, also referred to as t^* henceforth) observed for $k_s/D = 1.4 \times 10^{-3}$ at a Reynolds number of 1.64×10^{5} are given in the figure 8 (b, c & d respectively).

For $0 < t^* \leqslant 1200$, a stable LSB exists on both sides of the cylinder, which can be inferred from the lower mean C_D and mean C_L of ~ 0. The presence of the LSB delays separation, increases the base pressure and hence decreases C_D. For $t^* > 1200$, the LSB near $(\theta \sim (300° - 250°))$ becomes unstable and intermittent leading to increased C_D and a non-zero mean C_L. The onset of instability is found to occur over the entire span but since the LSB becomes intermittent, the separation line
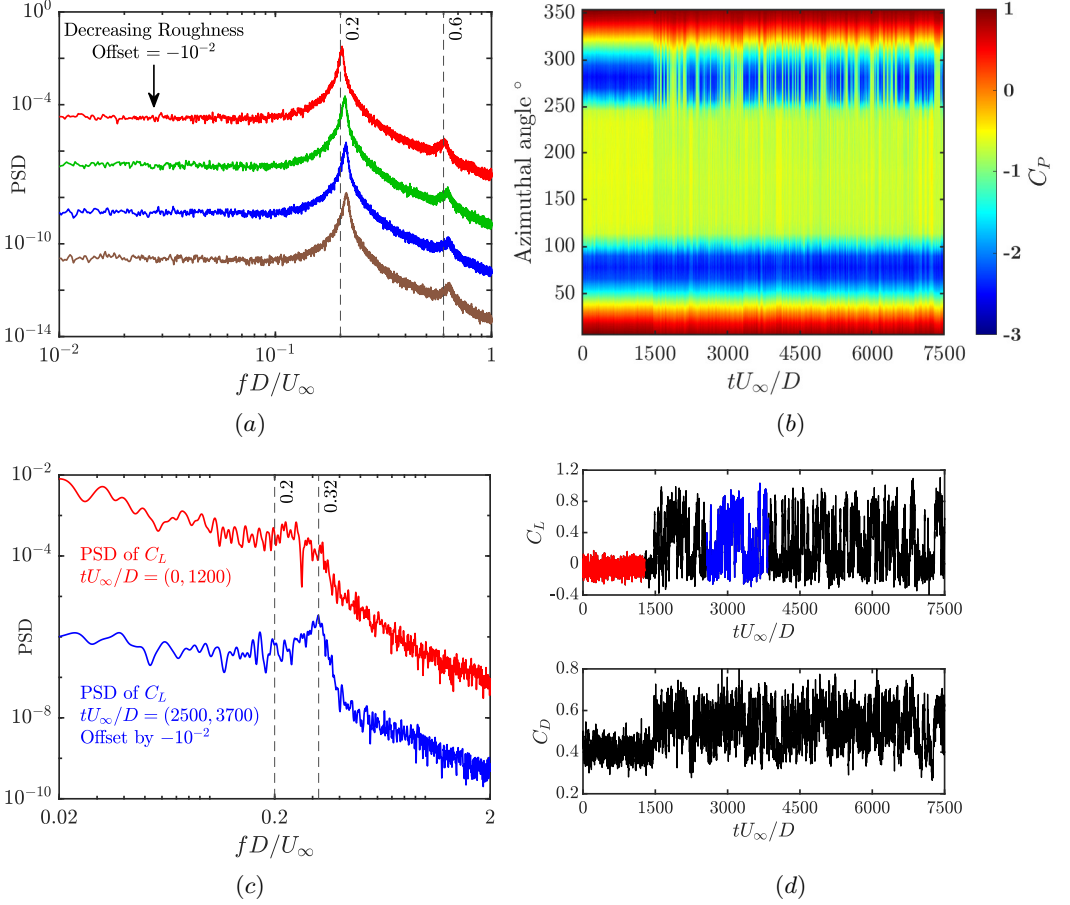
Figure 8. (*a*) Frequency spectra of the lift coefficient for different roughnesses at Reynolds number of 6.7×10^5. ——: $k_s/D = 3 \times 10^{-3}$, ——: $k_s/D = 1.9 \times 10^{-3}$, ——: $k_s/D = 1.4 \times 10^{-3}$ and ——: $k_s/D = 1.1 \times 10^{-3}$. (*b*) Coefficient of pressure versus time on $k_s/D = 1.4 \times 10^{-3}$ at Reynolds number of 1.64×10^5, (*c*) Spectra of C_L for different time intervals and (*d*) Time history of C_L and C_D of that test, and

in the spanwise direction at a given instant of time is expected to be jagged and hence, vortex shedding is incoherent (Bearman (1984)). This is also seen in the frequency spectra of the sectional lift coefficient from two different periods, $0 < t^* \leqslant 1200$ and $2500 < t^* \leqslant 3700$. A dominant frequency is present in the spectrum when the LSB is stable on both sides of the cylinder, while the spectrum resulting from an asymmetric intermittent LSB is broad range. The spectrum for the entire duration of the test ($t^* = 7500$, $t = 120s$) is broadband in nature and hence, these Reynolds numbers were excluded from figure 10 despite there being strong periodicity over a short period. In addition, the Strouhal number pertaining to the wake flow when there is a dominant frequency or a narrow band in the energy spectrum while in the 'two-bubble' state is higher than the Strouhal numbers in both sub-critical and post-critical regimes and is ~ 0.32. Bearman (1969) also found a higher frequency in the 'two-bubble' state.

This intermittent LSB is absent for the two rougher cylinders ($k_s/D = 1.9 \times 10^{-3}$ and $k_s/D = 3 \times 10^{-3}$) in the current tests. Thus, the prevalence of an
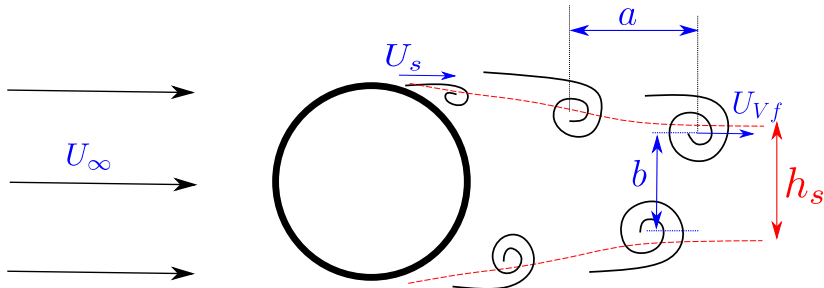
Figure 9. The length and velocity scales used in the calculation of universal strouhal numbers, St_R and St_B, **- - -**: Mean shear layers.

intermittent LSB reduces as the roughness is increased, i.e. the super-critical regime becomes smaller as the roughness is increased. In other words, surface roughness is found to promote coherent shedding in the Reynolds number space (in agreement with Achenbach & Heinecke (1981)).

The Strouhal number of the vortex shedding initially increases and then decreases with the Reynolds number, similar to the changes in wake angle and base pressure. This variation of Strouhal number with Reynolds number for different roughnesses is given in figure $10(a)$. For a given roughness, the Strouhal number decreases with an increasing Reynolds number in the post-critical flow, indicating that the wake width increases (Roshko (1961)). This increase is a consequence of the upstream movement of the separation angle and results in reduced base pressure and thus, increased drag. An increase in roughness at a given post-critical Reynolds number also increases wake width and hence decreases the Strouhal number. Current data also confirms the prediction of Achenbach & Heinecke (1981) that the post-critical Strouhal numbers for rough cylinders are smaller than those for smooth cylinders. In line with the asymptotic behaviour of separation angle, base pressure, and coefficient of drag, the Strouhal number eventually approaches asymptotic values at large Reynolds numbers (~ 0.2 for the roughest surface tested and ~ 0.21 for the smoothest).

Two proposed *universal Strouhal numbers*: the *Roshko* number, St_R, (Roshko (1954b, 1961)) and the *Bearman* number, St_B, (Bearman (1967)) were computed for the current tests and the results are presented in figure 10. While the Roshko number uses wake width and velocity near the separation point, the Bearman number makes use of lateral vortex separation and velocity near the separation point as the characteristic length and velocity scales, respectively. The Roshko number (Roshko (1954b)) is calculated as

$$St_R = \frac{f h_s}{U_s}, \tag{3.1}$$

where f is the frequency of shedding, U_s is the velocity at the edge of the boundary layer near the separation, and h_s is the lateral (cross-stream) spacing between the shear layers when they become parallel. U_s can be estimated through Bernoulli's equation as

$$U_s = U_\infty (1 - C_{P_b})^{0.5}.$$

From simple momentum considerations:

$$-C_{P_b} h_s = C_D D,$$

On the other hand, the Bearman number (Bearman (1967)) is

$$St_B = \frac{fb}{U_s} \tag{3.2}$$

where b is the lateral spacing between the centres of vortices of the same sign. f is the frequency of shedding, a is the longitudinal spacing between vortex centres. U_{Vb} is the velocity of vortex centres relative to the body (stationary cylinder in this investigation), U_{Vf} is the velocity of vortex centres relative to the freestream $(U_\infty = U_{Vf} + U_{Vb})$. From 3.2:

$$St_B = \frac{fba}{aU_\infty(1 - C_{P_b})^{0.5}},$$

$$fa = U_{Vb},$$

$$St_B = \frac{b}{a}\frac{U_{Vb}}{U_\infty}\frac{1}{(1 - C_{P_b})^{0.5}}. \tag{3.3}$$

Kronauer's stability criterion states that the vortex street aligns itself such that the vortex-street drag coefficient, C_{D_s}, is minimum with respect to the aspect ratio, b/a. This criterion can be simplified to

$$\frac{b}{a}\frac{U_{Vb}}{U_\infty} = F(C_D\,St). \tag{3.4}$$

where F is a function resulting from the stability criterion. Further information on the evaluation of the Bearman number is given in appendix §6.2.

Thus, the Roshko and the Bearman numbers for a given Reynolds number can be estimated using the coefficient of drag, C_D, the Strouhal number of shedding, St, and the base pressure coefficient, C_{P_b}. In these calculations of St_R and St_B, measured values (and not blockage-corrected ones) of C_D, St and C_{P_b} are used, since the influence of blockage and blockage corrections on the vortex street is uncertain (Bearman (1967)). The variation of St_R and St_B with Reynolds number for various roughnesses is given in figure 10(b).

St_B has less scatter than St_R over the range of Reynolds numbers and roughnesses tested. The values of St_R and St_B were found to be ~ 0.14 and ~ 0.17 in excellent agreement with those found by Adachi (1997) at similar Reynolds numbers on rough cylinders. The scatter in both St_R and St_B increases in the critical regime owing to uncertainties of measurements. Moreover, a slight downward trend in St_R is found with increasing Reynolds number suggesting that perhaps St_R is not truly universal. On the other hand, the variation in the post-critical regime is still small over the Reynolds number range considered but there is a noticeable spread with roughness. It is of note that the tests in the supercritical regime where periodic shedding is sporadic, are omitted in these calculations.

3.5. *Spanwise correlation of the lift*

The one-sided, axial correlation length of lift, Λ is determined following the procedure outlined in § 2.1 of Norberg (2003) and the results are given in the figure 11. A sample calculation for the correlation length is given in the appendix. Owing to the sparse spanwise distribution of pressure measurements, there is some scatter in the calculated axial correlation length. Despite the scatter, it is
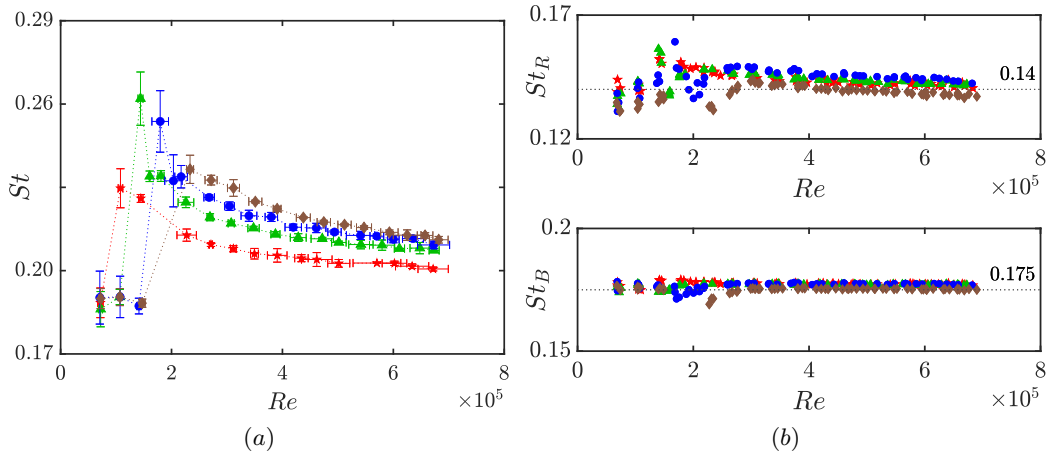
Figure 10. (*a*) Strouhal number, and (*b*) the Roshko number, St_R, (top) and the Bearman number, St_B, (bottom) for different roughnesses. Confidence intervals were calculated as described in §2.2. $\cdots\star\cdots$: $k_s/D = 3 \times 10^{-3}$, $\cdots\blacktriangle\cdots$: $k_s/D = 1.9 \times 10^{-3}$, $\cdots\bullet\cdots$: $k_s/D = 1.4 \times 10^{-3}$, $\cdots\blacklozenge\cdots$: $k_s/D = 1.1 \times 10^{-3}$.

clear that Λ doesn't vary significantly with roughness or Reynolds number in the post-critical regime. Broadly, Λ takes the value of $\sim 3D$ in the sub-critical regime and drops to $\sim 1.5D$ in the critical regime indicating a drop in coherence due to the intermittent separation. In the post-critical regime, Λ is $\sim 4D$ for all the roughnesses tested. These results are in excellent agreement with Buresti (1981) where correlation lengths were found using hot-wire measurements. This agreement is surprising given the difference in aspect ratios between the two setups and the method of measurement. As mentioned previously, correlation lengths of $\sim 3.2D$ and $\sim 3.9D$ were found at particular post-critical Re by Batham (1973) ($AR = 6.6$), Ribeiro (1991) ($AR = 6$), respectively, and the current results are in good agreement with them. However, Eaddy (2019) reported correlation lengths of $\sim 2.5 - 3.4D$ for an aspect ratio of 9 and $6D$ for an aspect ratio of 5.7. The turbulence intensity of the free stream in Eaddy (2019) was 4.4%, and this could be the cause of the slightly lower correlation lengths for the larger aspect ratio setup. It is interesting that an AR of 5.7 in Eaddy (2019), which is similar to that in Ribeiro (1991) and Batham (1973), resulted in a much higher correlation length. An increased blockage and vibration in their low aspect ratio setup could also contribute to this discrepancy. The difference in fluctuating lift coefficient between the two setups supports this hypothesis.

A correlation length of $\sim 4D$ thus appears to be the best estimate for post-critical flows over rough cylinders. This length is significantly larger than the $\Lambda \sim 1.5D$ for smooth cylinders at similar Reynolds numbers (Batham (1973); Blackburn & Melbourne (1996); King (1977)), indicating that the roughness increases spanwise uniformity of the flow in the Reynolds number range of $Re = 3 \times 10^5$ to 6.5×10^5. Schewe (1983) showed that the transition to the post-critical regime for smooth cylinders begins at $Re = 2.5 \times 10^6$. Hence, it is likely that the smooth cylinder results of correlation lengths at $3 \times 10^5 \leqslant Re \leqslant 6.5 \times 10^5$ were obtained in flow regimes that contain LSBs, thus explaining the lower correlation lengths. While the difference in axial correlation length of lift between smooth and rough cylinders at the same Reynolds number is significant, all roughnesses
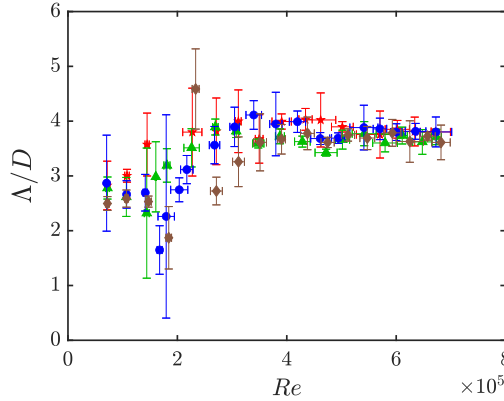
Figure 11. Axial correlation length of lift for different roughness and Reynolds numbers. Confidence intervals were calculated as described in §2.2. $\star$: $k_s/D = 3 \times 10^{-3}$, $\blacktriangle$: $k_s/D = 1.9 \times 10^{-3}$, $\bullet$: $k_s/D = 1.4 \times 10^{-3}$, $\blacklozenge$: $k_s/D = 1.1 \times 10^{-3}$.

tested showed similar correlation lengths implying that the magnitude of the roughness has little effect on the extent of spanwise correlation in the range of Reynolds numbers tested.

3.6. *On behaviour of the flow beyond $Re \sim \mathcal{O}(10^6)$*

The largest Reynolds number tested in the current work is 6.7×10^5 and all of the variables measured, i.e. C_D, σ_{C_L}, C_{P_b}, C_{P_m}, θ_w, St and Λ, appear to have reached or are close to their asymptotic values with respect to increasing Reynolds number. This observation is in agreement with that of Güven *et al.* (1980); Buresti (1981); Nakamura & Tomonari (1982) up to the largest Re tested in those works. Shih *et al.* (1993); Adachi (1997) investigated rough cylinders at Reynolds numbers up to $\mathcal{O}(10^7)$ and observed no evidence of the drag curve turning over as the Reynolds number was increased further towards the upper limit of those experiments.

On the other hand, the uncorrected drag coefficient, C_D in Achenbach (1971) for $k_s/D = 9 \times 10^{-3}$ decreased from ~ 1.3 at $Re \sim 3 \times 10^6$ to ~ 1.2 at $Re \sim 3 \times 10^7$. The magnitude of decrease in C_D was smaller in the blockage corrected drag coefficients, ~ 1.04 at $Re \sim 3 \times 10^6$ to ~ 1 at $Re \sim 3 \times 10^7$. In addition, van Hinsberg (2015) found that for larger Reynolds numbers, C_D, σ_{C_L}, St, and to a minor extent C_{P_b} and C_{P_m}, reached a peak before decreasing slightly beyond $Re \sim 10^6$. However, these trends were found to occur only with the data obtained from the flow generated through the larger total pressures (i.e., higher Mach numbers).

For a fixed diameter, larger Reynolds numbers result in larger Mach numbers, thus increasing the effect of compressibility of the working fluid. Jones *et al.* (1969) investigated Reynolds numbers from 0.4×10^6 to 14×10^6 on smooth cylinders at Mach numbers ranging from 0.1 to 0.6. C_D vs Re for Mach numbers above $M > 0.2$ showed the drag reaching a peak prior to remaining almost constant or decreasing slightly. Moreover, this behaviour was exacerbated at increasing Mach number. Thus, further investigations as $Re \rightarrow \mathcal{O}(10^7)$ over a range of Mach numbers are recommended to understand the influence of compressibility on different flow variables.

3.7. *The Roughness Reynolds number and curve collapse*

In post-critical flows, the influence of an increase in roughness is similar to that of an increase in Reynolds number, i.e. the minimum pressure, C_{P_m}, increases while base pressure, C_{P_b}, and wake angle, θ_w, decrease. From figure 6, it is also clear that C_{P_b} and θ_w approach asymptotic values with increasing roughness similar to the variation with increasing Reynolds number. The peak in the fluctuating pressure distribution moves upstream and σ_{C_P} in the downstream region of the cylinder increases with increasing roughness, and these changes too are qualitatively similar to those that occur with increasing Reynolds number. On the other hand, axial correlation length is $\sim 4D$ in the post-critical regime for all roughnesses tested and hence, the magnitude of spanwise correlation of forces is the same for all roughnesses tested in post-critical flow.

The variation in all the above-mentioned properties is similar whether it is a result of a change in Reynolds number or a change in roughness. This, combined with the difficulty of achieving post-critical Reynolds numbers while maintaining acceptable blockage and aspect ratio in most wind tunnels provides the support for the use of roughness to simulate the effect of post-critical flow proposed by Szechenyi (1975).

Figure 12 gives the variation of bulk properties, mean drag, and fluctuating lift as functions of Roughness Reynolds number, $Re_{k_s} = (\rho U_\infty k_s)/\mu = Re(k_s/D)$. In post-critical flows and for a given Roughness Reynolds number, the maximum deviation from the mean C_D among different roughnesses tested is only $\sim 3\%$. While the corresponding difference in the fluctuating coefficient of lift is higher (within 10%), this is of the order of the experimental error in predictions of σ_{C_L} as seen in figure 12(b).

Figure 13 gives the mean and fluctuating pressure distribution from different roughnesses at varying Reynolds numbers but at the same Roughness Reynolds number of 720. It is evident that the differences in mean C_P are only in the acceleration region and C_P nearby and post-separation is similar for all roughnesses. In the fluctuating pressure distribution, the peak of σ_{C_P} occurs near the same azimuthal angle. However, quantitative differences in σ_{C_P} in the downstream region are larger than those in the mean C_P and these contribute towards the differences in σ_{C_L}.

Mean base pressure, C_{P_b}, wake angle, θ_w, the total contribution of base C_P to the drag coefficient, $C_{D_{base}}$, and the contribution of upstream C_P to the drag coefficient, $C_{D_{rest}}$, Strouhal number, St, and the axial correlation length, Λ, are plotted against Roughness Reynolds number in figure 14. The wake angle, which, as previously described is representative of the separation angle in the post-critical regime, is fairly constant at a given Roughness Reynolds number irrespective of the roughness used to achieve it. C_{P_b} is a strong function of θ_w as seen in figure 6(f). Consequently, the base pressure and the contribution of the pressure distribution in the base region to drag is constant for a given Roughness Reynolds number. The contribution of the upstream region of drag is a function of roughness since flow in the acceleration region and C_{P_m} is a function of roughness even at large Reynolds numbers. However, this contribution is minor when compared to the contribution of base pressure, leading to only a minor deviation in the total drag coefficient.

Since the separation angle, drag coefficient and base pressure collapse with Roughness Reynolds number, it follows that wake parameters also collapse with
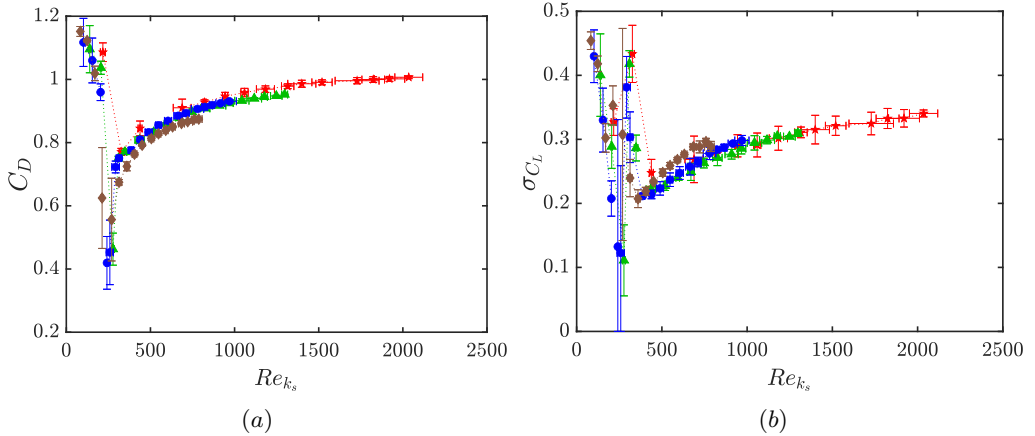
Figure 12. (a) Mean drag coefficient, and (b) Fluctuating lift coefficient as a function of Roughness Reynolds number. $\cdot\cdot\star\cdot\cdot$: $k_s/D = 3 \times 10^{-3}$, $\cdot\cdot\blacktriangle\cdot\cdot$: $k_s/D = 1.9 \times 10^{-3}$, $\cdot\cdot\bullet\cdot\cdot$: $k_s/D = 1.4 \times 10^{-3}$, $\cdot\cdot\blacklozenge\cdot\cdot$: $k_s/D = 1.1 \times 10^{-3}$.

Roughness Reynolds number thereby leading to a collapse of the Strouhal number. Strouhal number found from spectral peaks of the lift fluctuations is plotted against Roughness Reynolds number in figure 14(e).

To summarise, the mean drag coefficient and the Strouhal number collapse well when plotted against Roughness Reynolds number, since wake ($\sim$ separation) angle and consequently, base pressure, and wake width collapse with Roughness Reynolds number. On the other hand, the minimum pressure and the fluctuating lift coefficient are more sensitive to local flow perturbations, and hence different roughness levels and Reynolds numbers lead to differences in σ_{C_L}.

However, the asymptotic values of the base pressure, and the separation angle in post-critical flows for smooth cylinders (from Güven *et al.* (1980)) are different from those of rough cylinders in the current tests. A collapse of the drag coefficient with Roughness Reynolds number that includes data from smooth cylinders is hence expected to have a larger deviation than found by Güven *et al.* (1980). Moreover, axial correlation lengths for smooth cylinders in post-critical flows are unknown and the similarity among spanwise flow over smooth and rough cylinders in post-critical flows is still uncertain.

Thus, the use of Roughness Reynolds number is recommended in instances for which post-critical flow of a slightly rough cylinder is simulated using a rougher cylinder at a lower Reynolds number. Since the deviation in the collapse of C_D through Roughness Reynolds number is only from the minimum pressure region, this collapse would work well if the roughnesses tested have similar characteristics and cause similar deceleration in the flow. This explains the collapse of C_D observed in Szechenyi (1975) (since all the roughnesses were generated from glass beads) and the current work, and the deviations observed when different roughnesses were taken into account in Güven *et al.* (1980). The comparisons in Güven *et al.* (1980) were also from flow setups of different geometrical properties and investigations that attempt the curve collapse while incorporating different kinds of roughness elements in the same setup are required to further identify the limitations to the curve collapse using Roughness Reynolds number.

Szechenyi (1975) proposed three thresholds in the roughness simulation i.e., $Re_\delta \sim 200$ as the lower limit for the return of coherent vortex shedding, $Re_\delta \sim$
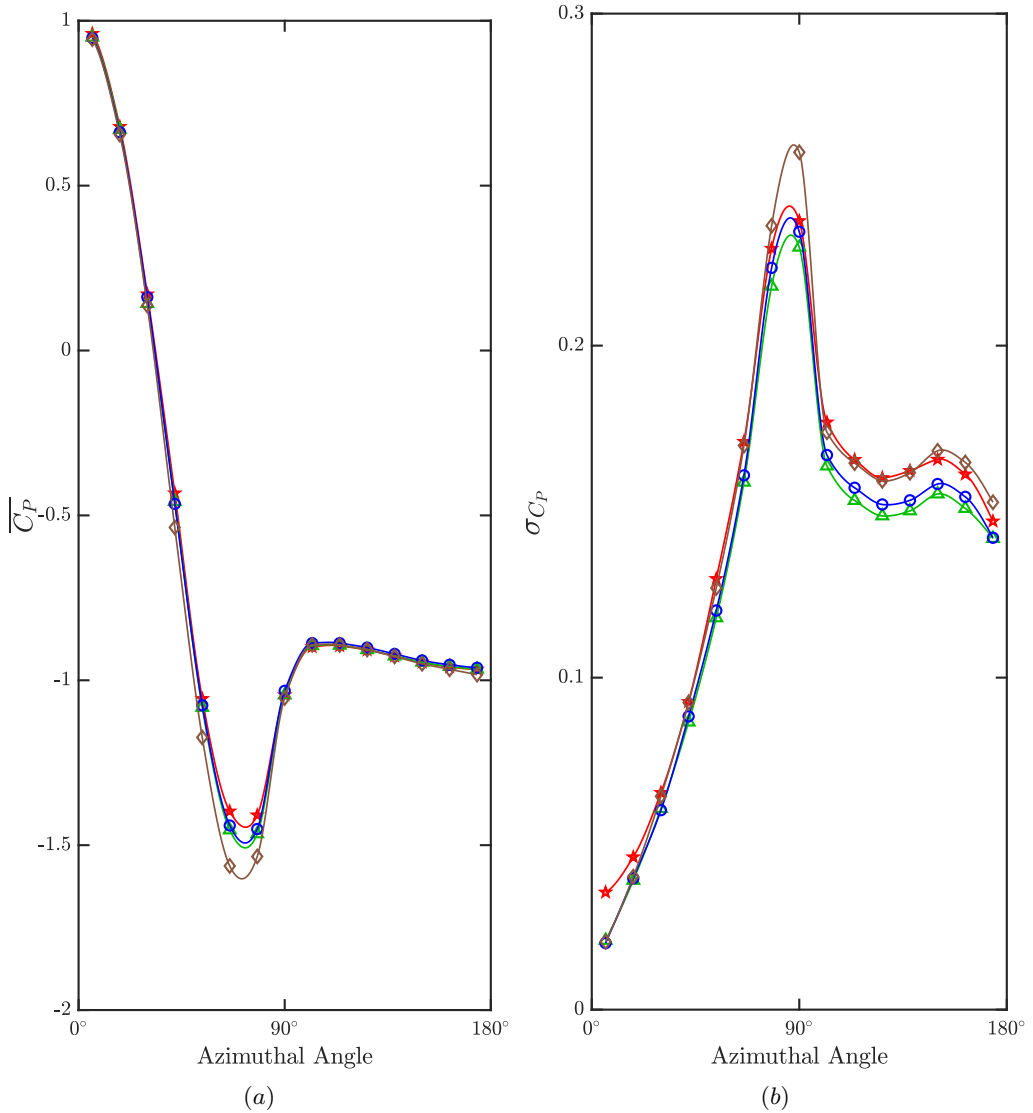
Figure 13. Circumferential distributions of (*a*) mean pressure and (*b*) fluctuating pressure coefficients at Roughness Reynolds number of 720. $\star$: $k_s/D = 3 \times 10^{-3}$, $\triangle$: $k_s/D = 1.9 \times 10^{-3}$, $\bigcirc$: $k_s/D = 1.4 \times 10^{-3}$, $\Diamond$: $k_s/D = 1.1 \times 10^{-3}$.

1000 as the lower limit after which the coefficients of drag, lift and the Strouhal number remain fairly constant, and a relative roughness ratio of $\delta/D = 2.2 \times 10^{-3}$ (where δ is the diameter of the glass beads used to generate roughness) as the upper limit after which the coherence in vortex shedding breaks down. For the roughnesses tested in the current study, the lower limit of Re_{k_s} at which the coherent shedding reestablishes intermittently is ~ 300 while the steady nature (i.e less uncertainity in the estimates) of the fluctuating lift coefficient, Strouhal number and the axial correlation length of lift are established at ~ 500. As mentioned previously, increase in roughness in the current experiments stabilises vortex shedding rather than disrupting it and coherent vortex shedding is seen
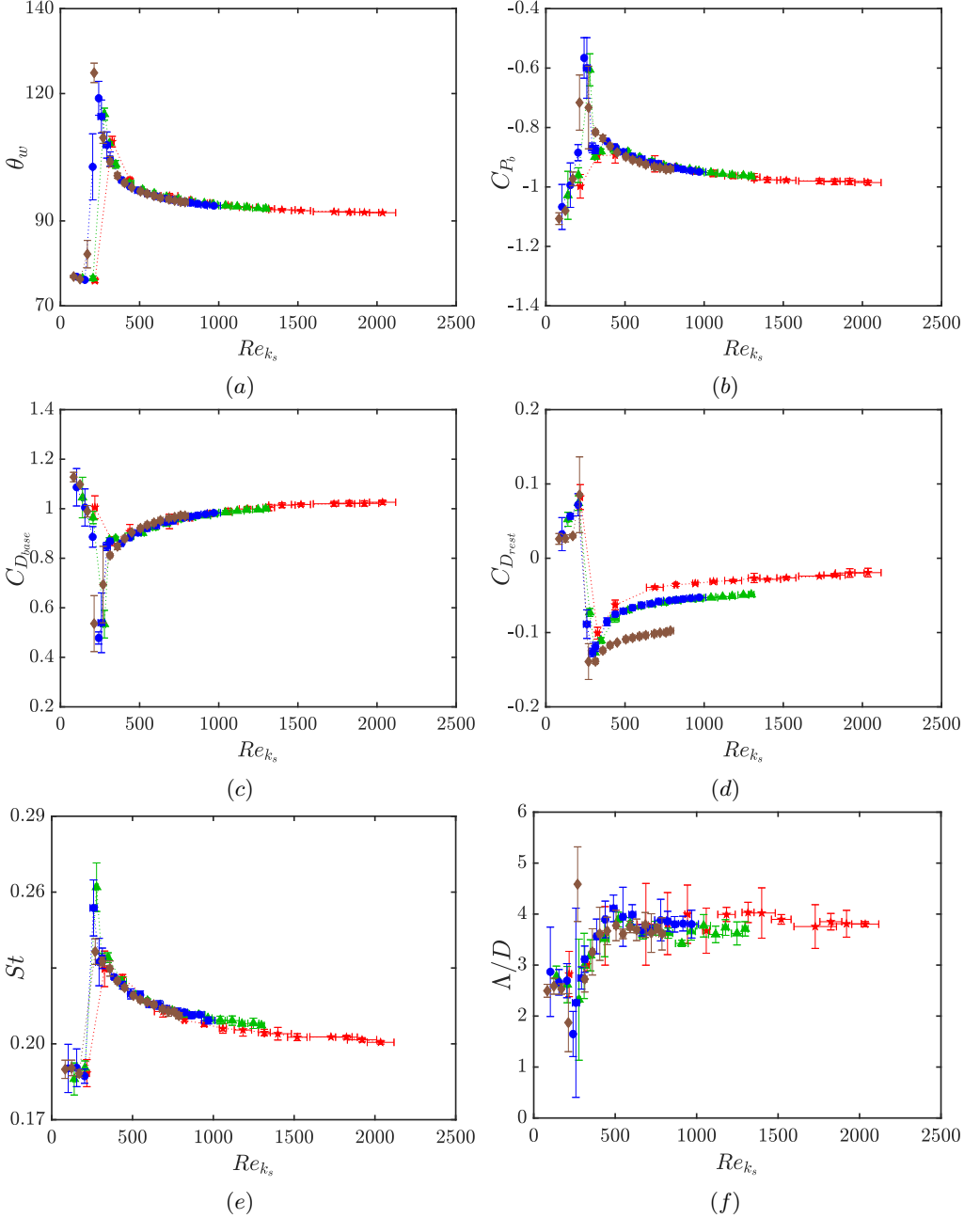
Figure 14. Variation of (a) Wake angle, (b) Base pressure coefficient, (c) Base pressure contribution, (d) Upstream pressure contribution to drag, (e) Strouhal number and (f) Axial correlation length of lift with roughness Reynolds number. $\cdots \star \cdots$: $k_s/D = 3 \times 10^{-3}$, $\cdots \blacktriangle \cdots$: $k_s/D = 1.9 \times 10^{-3}$, $\cdots \bullet \cdots$: $k_s/D = 1.4 \times 10^{-3}$, $\cdots \blacklozenge \cdots$: $k_s/D = 1.1 \times 10^{-3}$.

at all Reynolds numbers for relative roughness, $k_s/D = 3.1 \times 10^{-3}$. Moreover, Buresti (1981) found coherent shedding with relative roughness as high as $k/D = 12 \times 10^{-3}$. This discrepancy among the observations is probably due to the use of
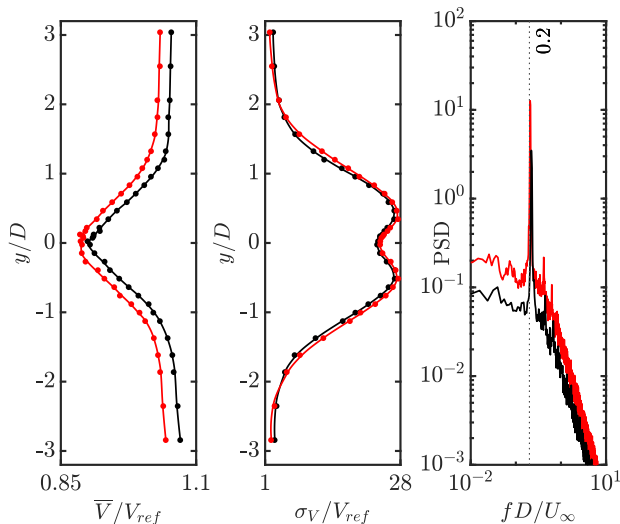
Figure 15. Mean, fluctuating in-plane velocity distribution and spectra of fluctuations at point of maximum σ_V in the wake of the cylinder of roughness, $k_s/D = 3 \times 10^{-3}$. ——: $Re \sim 1.9 \times 10^5$, ——: $Re \sim 3.8 \times 10^5$

glass beads in Szechenyi (1975) to generate roughness while sandpaper was used in Buresti (1981) and the current experiments.

3.8. *Intermediate wake measurements*

Mean and fluctuating velocity profiles and the power spectral density of velocity at 3 diameters downstream of the 40 grit cylinder are given in figure 15. These are measured using a single-axis hot-film anemometer with its axis parallel to the axis of the cylinder and hence, the hot wire is sensitive to the total in-plane velocity. This total in-plane velocity is denoted by V while y is the cross-stream distance from the centre of the cylinder.

For a fixed roughness, the mean velocity in the wake decreases with an increase in Reynolds number and this increase in the velocity deficit leads to higher drag. Fluctuations in the velocity increase with increasing Reynolds number, albeit at a lower rate than the mean velocity. Power spectra of the velocity fluctuations (at the point at which fluctuating velocity is maximum) show that energy content over the entire frequency range is higher for the larger Reynolds number tested. Similar to the observation from C_L spectra, Strouhal number of the dominant frequency decreases slightly as the Reynolds number increases in the post-critical regime.

Velocity profiles and spectra downstream of two different roughnesses but at the same Reynolds number are given in figure 16. The mean velocity deficit is similar for the two roughnesses while the wake width is slightly smaller for the lower roughness. Consistent with the fluctuating lift coefficient, σ_{C_L}, and the fluctuating coefficient of pressure, σ_{C_P}, the fluctuating velocity shows a clear increase with increasing roughness, indicating an increase in the turbulent kinetic energy. While the energy density over the broad frequency range is similar for both roughnesses, the dominant shedding frequency has more energy for the larger roughness, possibly because this roughness is well into the post-critical regime. This shows that at a given Reynolds number, energy fluctuations are larger for
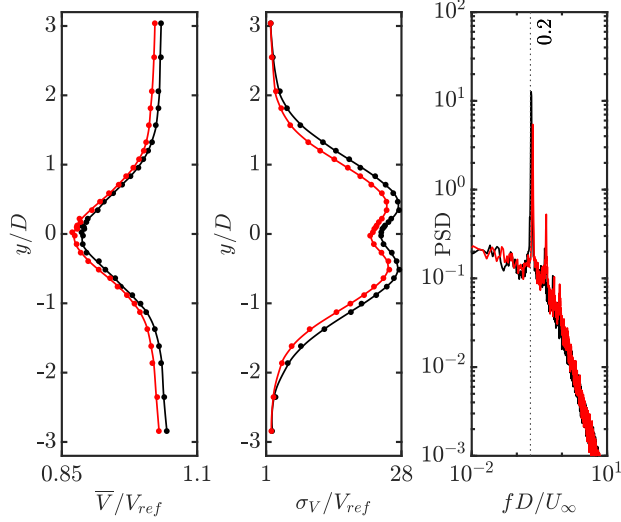
Figure 16. Mean, fluctuating in-plane velocity distribution and spectra of fluctuations at point of maximum σ_V in the wake at, $Re \sim 3.8 \times 10^5$. ——: $k_s/D = 3 \times 10^{-3}$, ——: $k_s/D = 1.1 \times 10^{-3}$
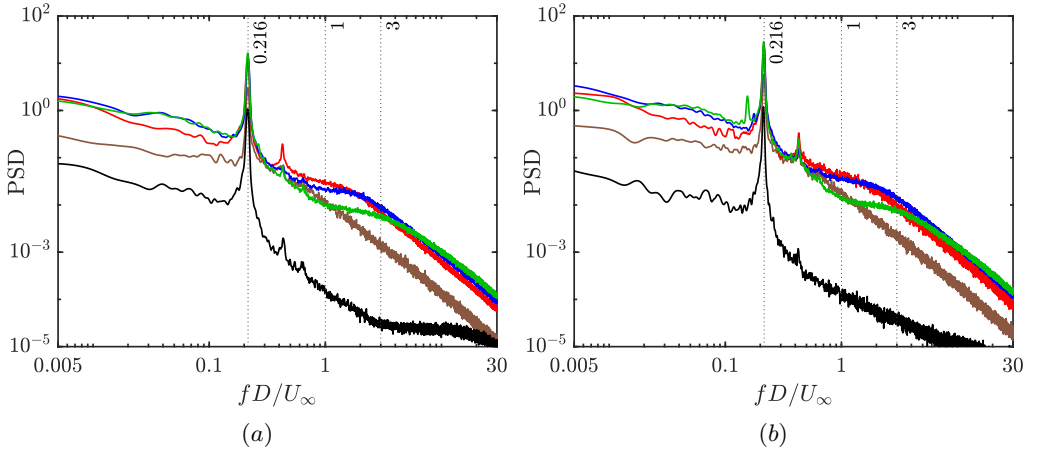

Figure 17. Frequency spectra of velocity fluctuations in the wake. (a) $k_s/D = 1.9 \times 10^{-3}$ at $Re = 2.9 \times 10^5$ & $Re_{k_s} = \sim 550$, and (b) $k_s/D = 1.1 \times 10^{-3}$ at $Re = 4.7 \times 10^5$ & $Re_{k_s} = \sim 510$. Spectra obtained at the location of the cross-stream maximum velocity fluctuation at ——: 0D, ——: 0.25D, ——: 0.5D, ——: 1D, ——: 6D downstream from the centre of the cylinder.

the larger roughness and that the increased energy is concentrated predominantly at the shedding frequency.

Wake profiles for the cylinders with relative roughness $k_s/D = 1.9 \times 10^{-3}$ and $k_s/D = 1.1 \times 10^{-3}$ through the near and intermediate wake are given in the appendix.

3.9. *Wake frequencies*

Figure 17 shows the power spectral density of velocity fluctuations at different downstream locations in the wake for two roughnesses, $k_s/D = 1.9 \times 10^{-3}$ and $k_s/D = 1.1 \times 10^{-3}$, at $Re_{k_s} \sim 550$. At each of these locations, a spectrum is obtained from the time history of in-plane velocity at a point where σ_V/V_{ref} is

Relative roughness k_s/D	Re	Θ/D at $(x/D = 0.25)$	Θ/D at $(x/D = 0.5)$
1.4×10^{-3}	2.9×10^{5}	0.0092	0.0212
1.4×10^{-3}	3.8×10^{5}	0.0112	0.0239
1.1×10^{-3}	3.8×10^{5}	0.0068	0.0203
1.1×10^{-3}	4.7×10^{5}	0.0092	0.0224

Table 3. Momentum thickness (Θ/D) of the shear layer at different streamwise locations.

maximum in the cross-stream profile. The energy in fluctuations before separation is lower than that post-separation over the entire frequency range. Spectra in the shear layer (at $0.25D$, $0.5D$ and $1D$) have the highest energy among the measurement range, and moreover, a plateau in the power spectral density is found at higher frequencies of $fD/U_\infty \sim 1 - 3$. These frequencies also had a higher spatial amplification factor, α, (Khor *et al.* (2011)) confirming that these are the frequencies at which shear-layer instabilities grow fastest. Furthermore, as one moves downstream, the frequency in the shear layers reduces slightly indicating an increase in shear-layer thickness. A similar plateau is found at post-critical Reynolds numbers for smooth cylinders in Lehmkuhl *et al.* (2014) and was considered a signature of Kelvin-Helmholtz frequencies, f_{KH}, in the shear layer. While shear-layer frequencies in the smooth cylinder follow the power law suggested by Prasad & Williamson (1997) ($f_{KH}/f_V \propto Re^{0.67}$), f_{KH} in the current results is an order of magnitude lower for the same Reynolds number. For instance, at a Reynolds number of 3.8×10^5, the power law for smooth cylinders predicts $f_{KH}D/U_\infty \sim 30$ while the current results show the broad-band frequency between $1 - 3$.

To further investigate this deviation, the momentum thickness of the shear layer, Θ was computed according to the procedure outlined in Khor *et al.* (2011) and the results are tabulated in table 3. Since the hot film anemometer measures the total in-plane velocity, current values of momentum thickness are expected to be only approximate. The key takeaway however, is that the momentum thickness of the shear layers for rough cylinders is an order of magnitude higher than that of the predicted smooth-cylinder momentum thickness, ~ 0.003 at $0.5D$ according to the correlation given in Khor *et al.* (2011) at the same Reynolds number. Since the boundary-layer thickness is larger on rough surfaces than on smooth surfaces for a given post-critical Reynolds number, separated shear layers are also expected to be thicker.

The empirical power-law correlations of f_{KH} and Θ/D versus Re for smooth cylinder flows don't contain data from the post-critical regime where shear layers are expected to be turbulent and hence, thicker than laminar shear layers. Moreover, as the Reynolds number increases, the energy content of the turbulent shear layer is expected to be distributed over a wider range of frequencies thereby making it difficult to discern an exact value for f_{KH}. However, current predictions of momentum thickness agree remarkably well with those of shear-layer frequencies when the inverse proportionality between the frequency and shear-layer thickness is taken into account, i.e. while the frequency peak of shear layers is an order of magnitude smaller than that obtained from the smooth cylinder correlations, the momentum thickness is an order of magnitude larger.

4. Conclusions

This study draws new insights into the aerodynamic behaviour of roughened cylinders at post-critical Reynolds numbers and elucidates prior inconsistencies in the literature for this flow. We present a new consistent, reliable, and comprehensive data-set that minimises the confounding effects of blockage and aspect ratios, and the variability they can induce. The motivation for this study was the variable and sometimes contradictory conclusions drawn from a number of previous studies on rough cylinders at high Reynolds numbers, making it difficult to use prior literature findings for reliable prediction and application.

This work consists of wind tunnel experiments covering the pre-critical to the post-critical Reynolds number range based on cylinders of aspect ratio, $AR = 9.8$ positioned in a wind tunnel with a blockage ratio of 5%. We quantify the key parameters of the flow such as the drag and lift coefficients, circumferential pressure distributions and their corresponding spectra, and the axial correlation length of lift for relative roughness ratios, $1.1 \times 10^{-3} \leqslant k_s/D \leqslant 3 \times 10^{-3}$, and Reynolds numbers, $0.5 \times 10^5 \leqslant Re \leqslant 6.7 \times 10^5$. Analysis of these results leads to several important findings:

(i) Corrections to the influence of wind tunnel walls work well for the mean drag coefficient, C_D. The blockage corrected drag coefficients from the current work are in good agreement with those from Achenbach & Heinecke (1981); Güven *et al.* (1980); van Hinsberg (2015) despite widely varying blockage. On the other hand, there is a non-negligible scatter in parameters like C_{P_b} & C_{P_m} across different investigations. This difference brings into question the applicability of blockage corrections to C_P, especially at large blockages ($> 15\%$) found in Güven *et al.* (1980) and Achenbach & Heinecke (1981).

(ii) Moreover, Eaddy (2019) found a large ($\sim 30\%$) increase in σ_{C_L} for an increase in aspect ratio from 5.7 to 9 and blockage from 8% to 12%. The blockage corrections to the fluctuating coefficient haven't been verified yet thereby necessitating the use of a low blockage and high aspect ratio setup in order to get accurate measurements of the fluctuating coefficient of lift.

(iii) We present, for the first time, the fluctuating lift coefficient, σ_{C_L} for a range of surface roughnesses in the post-critical flows measured through a low blockage and high aspect ratio setup. Despite having similar geometrical parameters (and similar C_D), current results of σ_{C_L} vary significantly from those of van Hinsberg (2015) for a similar relative roughness. Possible causes of the discrepancy are the differences in the method of generation of surface roughness, the measurement technique along with the influence of gaps between the tunnel walls and the cylinder present in the setup of van Hinsberg (2015).

(iv) This study reveals a strong correlation between the separation angle (quantified through wake angle, θ_w) and the base pressure (quantified through C_{P_b}) of the cylinder in the post-critical regime that is consistent across the range of roughnesses tested. The wake angle, θ_w, and consequently, the base pressure, C_{P_b}, Strouhal number, St, and the coefficient of drag, C_D, decrease with increasing Reynolds number for a given roughness in the post-critical regime. On the other hand, minimum pressure, C_{P_m}, and the fluctuating coefficient of lift, σ_{C_L}, increase with increasing Reynolds number. These quantities eventually approach asymptotic values at large Reynolds numbers. Amongst these quantities, only the asymptotic value of C_{P_m} strongly depends on the degree of roughness and is not well described by only the Roughness Reynolds number. Measurements by Jones

et al. (1969) in a pressurised wind tunnel suggest that at very high Reynolds numbers the drag coefficient could reach a maximum and then decrease slightly as the Reynolds number is increased further. This might be caused by compressibility effects since the Mach number was not negligible in those experiments. Further studies at very large Reynolds numbers ($\sim 10^7$) and different Mach numbers are recommended to understand the influence of compressibility better.

(v) Time histories and frequency spectra of the lift signal revealed that intermittency of the LSB disturbs coherent vortex shedding and no dominant frequency exists in such a flow. This super-critical flow is found to occur over a smaller range of Reynolds number as roughness increases, i.e. coherent (spanwise) and periodic vortex shedding exists over a larger Reynolds number space for higher roughness. A distinct frequency in shedding is found at all the Reynolds numbers tested for a cylinder with relative surface roughness $k_s/D \geqslant 1.9 \times 10^{-3}$ but not for $k_s/D \leqslant 1.4 \times 10^{-3}$ at Reynolds numbers near $Re \sim 2 \times 10^5$.

(vi) This study reports the axial correlation length of lift for a range of roughnesses at Reynolds numbers $Re \leqslant 6.7 \times 10^5$. In excellent agreement with the broad estimates of Buresti (1981), the axial correlation length, Λ, at $Re \geqslant 3 \times 10^5$ is $\sim 4D$ for all roughnesses tested. This length is significantly higher than that for smooth cylinders ($\sim 1.5D$) at similar Reynolds numbers (King (1977)) indicating an earlier re-establishment of coherent shedding with increasing roughness.

(vii) This work also quantifies the velocity distributions in the wake of rough cylinders in post-critical flows. We show that the flow velocity at 3 diameters downstream of the cylinder decreases as the Reynolds number or roughness is increased. For a given Reynolds number, the velocity in the wake recovers faster in the streamwise direction for the lower roughness.

(viii) Momentum thickness of the shear layer for rough cylinders is found to be $\Theta/D \sim 0.02$ at 0.5D downstream of the cylinder. This is an order of magnitude higher than that of empirically predicted momentum thickness for smooth cylinders at the same Reynolds numbers. Consequently, the frequencies in the shear layer post-separation for the rough cylinder are found at $f_{KH}D/U_\infty \sim 2-3$, an order of magnitude lower than the smooth cylinder predictions.

(ix) Flow properties such as C_D, σ_{C_L}, C_{P_b} are plotted against the Roughness Reynolds number, Re_{k_s} for different roughnesses, the conclusions are:

    (a) Across the range of surface roughness tested, the wake angle follows a consistent trend with the Roughness Reynolds number. The strong correlation between the wake angle and base pressure leads to a collapse of base pressure. This further results in a collapse of the Strouhal number and the drag coefficient with the Roughness Reynolds number.

    (b) The deviation in the mean drag coefficient, C_D, among different roughnesses is within 3% of the mean C_D for the range of Roughness Reynolds number considered. The major contribution for the C_D collapse is from the agreement of base pressure between different roughnesses at the same Roughness Reynolds number (indicated by the collapse of C_{P_b} with Re_{k_s}), while the deviation is due to differences in the degree of deceleration before separation caused by different roughness (represented by C_{P_m}).

    (c) The correlation of σ_{C_L} with Re_{k_s} is more consistent (deviation within $\sim 10\%$ of the mean of different roughness) than that reported by Szechenyi (1975), and Eaddy (2019). Geometrical differences in the setups used by those authors are the likely cause of this discrepancy. In particular, it

appears that low cylinder aspect ratio and high blockage ratio play an important role.

(d) The similarity parameter to collapse variables in the current study is $Re_{k_s} = Re\,(k_s/D)$, which is different from the $Re\,(k/D)^{0.6}$ dependence proposed by Nakamura & Tomonari (1982). On this point, Nakamura & Tomonari (1982) used polystyrene particles to generate the distributed roughness and adopted the roughness parameter, k, as the size of roughness particles, while the current study makes use of sandpaper and uses the equivalent sand-grain roughness, k_s. This difference could be the cause of the difference between the two similarity parameters, but this aspect should be investigated further.

(e) Reynolds numbers of large engineered structures or even their components are often difficult to achieve in standard wind tunnels while maintaining acceptable blockage and aspect ratios. Current results support the argument that, with the knowledge of surface roughness and Reynolds numbers for real-life structures of interest, a similar flow scenario can be achieved in wind tunnels at a much lower Reynolds number provided that roughness is tuned to match the Roughness Reynolds number (within the range of $Re \lesssim 7 \times 10^5$ and $1.1 \times 10^{-3} \leqslant k_s/D \leqslant 3 \times 10^{-3}$).

5. Acknowledgments

REFERENCES

ACHENBACH, ELMAR 1971 Influence of surface roughness on the cross-flow around a circular cylinder. *Journal of Fluid Mechanics* **46** (2), 321–335.

ACHENBACH, E. & HEINECKE, E. 1981 On vortex shedding from smooth and rough cylinders in the range of Reynolds numbers $6{\times}10^{3}$ to $5{\times}10^{6}$. *Journal of Fluid Mechanics* **109**, 239–251.

ADACHI, TSUTOMU 1997 Effects of surface roughness on the universal Strouhal number over the wide Reynolds number range. *Journal of Wind Engineering and Industrial Aerodynamics* **69-71**, 399–412.

AKIMA, HIROSHI 1970 A new method of interpolation and smooth curve fitting based on local procedures. *Journal of the ACM* **17** (4), 589–602.

ALLEN, H.J. & VINCENTI, W.G. 1944 Wall interference in a two-dimensional-flow wind tunnel, with consideration for the effect of compressibility. *NACA Technical Report* .

AUBERTINE, CAROLYN D., EATON, JOHN K. & SONG, SIMON 2004 Parameters controlling roughness effects in a separating boundary layer. *International Journal of Heat and Fluid Flow* **25** (3), 444–450, turbulence and Shear Flow Phenomena (TSFP-3).

BASU, R.I. 1985 Aerodynamic forces on structures of circular cross-section. Part 1. model-scale data obtained under two-dimensional conditions in low-turbulence streams. *Journal of Wind Engineering and Industrial Aerodynamics* **21** (3), 273–294.

BATHAM, J. P. 1973 Pressure distributions on circular cylinders at critical Reynolds numbers. *Journal of Fluid Mechanics* **57** (2), 209–228.

BEARMAN, P. W. 1967 On vortex street wakes. *Journal of Fluid Mechanics* **28** (4), 625–641.

BEARMAN, P. W. 1969 On vortex shedding from a circular cylinder in the critical Reynolds number regime. *Journal of Fluid Mechanics* **37** (3), 577–585.

BEARMAN, P W 1984 Vortex shedding from oscillating bluff bodies. *Annual Review of Fluid Mechanics* **16**, 195–222.

BERGH, H. & TIJDEMAN, H. 1965 Theoretical and experimental results for the dynamic response of pressure measuring systems. *Nationaal Lucht- en Ruimtevaartlaboratorium* .

BLACKBURN, H M & MELBOURNE, W H 1996 The effect of free-stream turbulence on sectional lift forces on a circular cylinder. *Journal of Fluid Mechanics* **306**, 267–292.

BRUNN, H.H 1995 *Hot-wire anemometry*. Oxford University Press.

BURESTI, GUIDO 1981 The effect of surface roughness on the flow regime around circular cylinders. *Journal of Wind Engineering and Industrial Aerodynamics* **8** (1), 105–114.

CADOT, O., DESAI, A., MITTAL, S., SAXENA, S. & CHANDRA, B. 2015 Statistics and dynamics of the boundary layer reattachments during the drag crisis transitions of a circular cylinder. *Physics of Fluids* **27** (1), 014101.

CHAKROUN, W.M., RAHMAN, A.A. ABDEL & QUADRI, M.M.A. 1997 The effect of surface roughness on flow around a circular cylinder. *Wind Engineering* **21** (1), 1–12.

CHEUNG, J & MELBOURNE, W 1995 Effects of surface roughness on a circular cylinder in supercritical turbulent flow. *Twelfth Australasian Fluid Mechanics Conference* pp. 25–28.

DUARTE RIBEIRO, JOSÉLUIS 1992 Fluctuating lift and its spanwise correlation on a circular cylinder in a smooth and in a turbulent flow: a critical review. *Journal of Wind Engineering and Industrial Aerodynamics* **40** (2), 179–198.

EADDY, MICHAEL 2019 Lift forces on smooth and rough circular cylinders in low and high turbulence flows. *DOI:10.26180/5dccbeae99c1f* .

FAGE, A., A.R.C.SC. & WARSAP, J. H. 1929 The effects of turbulence and surface roughness on the drag of a circular cylinder. *Reports and Memoranda No.1283, Aeronautical Research Committee* .

FARELL, CÉSAR, CARRASQUEL, SAUL, GÜVEN, OKTAY & PATEL, V. C. 1977 Effect of wind-tunnel walls on the flow past circular cylinders and cooling tower models. *Journal of Fluids Engineering* **99** (3), 470–479.

FOX, T A & WEST, G S 1990 On the use of end plates with circular cylinders. *Experiments in Fluids* **9** (4), 237–239.

FREYMUTH, P 1977 Frequency response and electronic testing for constant-temperature hot-wire anemometers. *Journal of Physics E: Scientific Instruments* **10** (7), 705.

GÜVEN, O., FARELL, C. & PATEL, V. C. 1980 Surface-roughness effects on the mean flow past circular cylinders. *Journal of Fluid Mechanics* **98** (4), 673–701.

JONES, G.W., CINCOTTA, J.J. & WALKER, R.W. 1969 Aerodynamic forces on a stationary and oscillating circular cylinder at high Reynolds numbers. *N.A.S.A Tech Rep R-300* .

KACKER, S. C., PENNINGTON, B. & HILL, R. S. 1974 Fluctuating lift coefficient for a circular cylinder in cross flows. *Journal of Mechanical Engineering Science* **16** (4), 215–224.

KHOR, M., SHERIDAN, J. & HOURIGAN, K. 2011 Power-spectral density estimate of the Bloor-Gerrard instability in flows around circular cylinders. *Experiments in Fluids* **50** (3), 527–534.

KING, ROGER 1977 A review of vortex shedding research and its application. *Ocean Engineering* **4** (3), 141–171.

LEHMKUHL, O., RODRÍGUEZ, I., BORRELL, R., CHIVA, J. & OLIVA, A. 2014 Unsteady forces on a circular cylinder at critical Reynolds numbers. *Physics of Fluids* **26** (12), 125110.

MILNE-THOMSON, L. M. 1962 *Theoretical Hydromechanics*. Macmillan & CO LTD.

NAKAMURA, Y. & TOMONARI, Y. 1982 The effects of surface roughness on the flow past circular cylinders at high Reynolds numbers. *Journal of Fluid Mechanics* **123**, 363–378.

NIKURDASE, J. 1933 Stromungsgesetze in rauhen rohren. *Forsch. Arb. 1ng.-Wes. Heft* .

NORBERG, C. 2003 Fluctuating lift on a circular cylinder: review and new measurements. *Journal of Fluids and Structures* **17** (1), 57–96.

PRASAD, ANIL & WILLIAMSON, CHARLES H. K. 1997 The instability of the shear layer separating from a bluff body. *Journal of Fluid Mechanics* **333**, 375–402.

RIBEIRO, J L D 1991 Effects of surface-roughness on the 2-dimensional flow past circular cylinders 1. mean forces and pressures. *Journal of Wind Engineering and Industrial Aerodynamics* **37** (3), 299–309.

ROSHKO, ANATOL 1954b On the drag and shedding frequency of two-dimensional bluff bodies. *Nat. Adv. Comm. Aero. Wash. Tech. Note, no.* **TN-3169**.

ROSHKO, ANATOL 1961 Experiments on the flow past a circular cylinder at very high Reynolds number. *Journal of Fluid Mechanics* **10** (3), 345–356.

SCHEWE, GÜNTER 1983 On the force fluctuations acting on a circular cylinder in crossflow from subcritical up to transcritical Reynolds numbers. *Journal of Fluid Mechanics* **133**, 265–285.

SHIH, W C L, WANG, C, COLES, D & ROSHKO, A 1993 Experiments on flow past rough circular cylinders at large Reynolds numbers. *Journal of Wind Engineering and Industrial Aerodynamics* **49** (1-3), 351–368.

SONG, S. & EATON, J. 2002 The effects of wall roughness on the separated flow over a smoothly contoured ramp. *Experiments in Fluids* **33** (1), 38–46.

SPEIDEL, L 1954 Einfluß der oberflächenrauhigkeit auf die strömungsverluste in ebenen schaufelgittern. *Forschung auf dem Gebiet des Ingenieurwesens A* **20**, 129–140.

STANSBY, P K 1974 The Effects of End Plates on the Base Pressure Coefficient of a Circular Cylinder. *Aeronautical Journal* **78 , 757** (January), 0–1.

SZECHENYI, EDMOND 1975 Supercritical Reynolds number simulation for two-dimensional flow over circular cylinders. *Journal of Fluid Mechanics* **70** (3), 529–542.

THOMPSON, M. C. & HOURIGAN, K. 2005 The shear layer instability of a circular cylinder wake. *Physics of Fluids* **17** (2), 021702 (4 pages).

VAN HINSBERG, NILS PAUL 2015 The Reynolds number dependency of the steady and unsteady loading on a slightly rough circular cylinder: From subcritical up to high transcritical flow state. *Journal of Fluids and Structures* **55**, 526–539.

ZAN, S.J. & MATSUDA, K. 2002 Steady and unsteady loading on a roughened circular cylinder at Reynolds numbers up to 900,000. *Journal of Wind Engineering and Industrial Aerodynamics* **90** (4), 567–581.
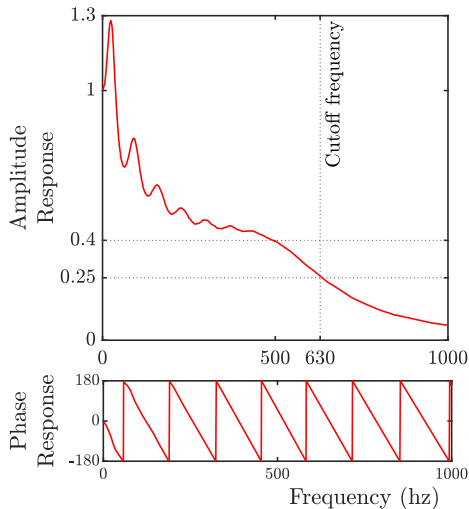
Figure 18. Transfer function applied to the pressure measurements.

6. Appendix

6.1. *Transfer function used for pressure measurements*

Figure 18 gives the transfer function calculated based on the length of the tube used to measure the pressure signal (from Bergh & Tijdeman (1965)). This transfer function is applied to all the pressure measurements in the current investigation.

6.2. *Evaluating axial correlation length of lift*

Figure 19 gives the coefficient of correlation between the fluctuations of lift coefficients measured at different spanwise locations. The correlation coefficient is defined as

$$R(s) = \frac{\Sigma \left(C_L(0) - \overline{C_L(0)} \right) \left(C_L(s) - \overline{C_L(s)} \right)}{\sqrt{\Sigma \left(C_L(0) - \overline{C_L(0)} \right)^2} \sqrt{\Sigma \left(C_L(s) - \overline{C_L(s)} \right)^2}}, \qquad (6.1)$$

where Σ indicates the summation over all the time steps in the duration of the test, $\overline{C_L}$ indicates the time average lift coefficient in that test, C_L is the instantaneous lift coefficient at each time step, $C_L(0)$ indicates the lift coefficient at the reference position (measurement plane at $-1D$) and $C_L(s)$ indicates the lift coefficient at the same instant measured at a spanwise separation of s.

A model function is fit over the discrete spanwise measurements in order to estimate the axial correlation length of lift. This function is given by (Norberg 2003)

$$R(s) = \alpha \exp\left(\frac{-s}{\Lambda_1} \right) + (1 - \alpha) \left(1 + \left(\frac{s}{C\Lambda_2} \right)^n \right)^{-1}, \qquad (6.2)$$

where C is $sin(\pi/n)/(\pi/n)$.

For each of the tests, 6.2 is used as a curve fit to the correlation functions by
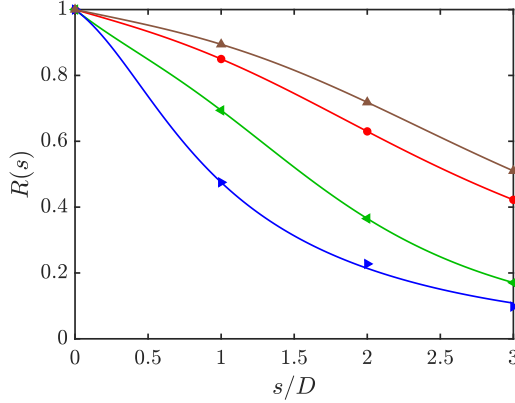
Figure 19. Correlation between the lift coefficients measured at different spanwise locations. Surface roughness, $k_s/D = 1.4 \times 10^5$, ——: $Re \sim 0.7 \times 10^5$, ——: $Re \sim 1.64 \times 10^5$ (same test as figure 8), ——:$Re \sim 1.68 \times 10^5$, ——:$Re \sim 6.4 \times 10^5$.

varying α, Λ_1, Λ_2 and n. The axial correlation length is then determined by

$$\Lambda = \alpha(\Lambda_1) + (1 - \alpha)(\Lambda_2). \tag{6.3}$$

For instance, the correlation lengths for the distributions in the figure 19 are $3.4, 1.9, 1.4$ and 3.8, respectively, for the range of Reynolds number provided. Figure 19 also highlights the uncertainty associated with the flow configuration in the super-critical regime.

6.3. *Evaluating the Bearman number*

From the potential flow model, the vortex drag coefficient, C_{D_S}, caused by two rows of staggered point vortices is given by (Bearman 1967; Milne-Thomson 1962)

$$C_{D_S} = \frac{4}{\pi} \left(\frac{U_{Vf}}{U_\infty}\right)^2 \left[\coth^2 \frac{\pi b}{a} + \left(\frac{U_\infty}{U_{Vf}} - 2\right) \frac{\pi b}{a} \coth \frac{\pi b}{a}\right], \tag{6.4}$$

where

$$C_{D_S} = \frac{D_S}{0.5\rho U_\infty^2 a}. \tag{6.5}$$

Here, a and b are the longitudinal (streamwise) and lateral (cross-stream) separations of the vortices, and $U_\infty = U_{Vb} + U_{Vf}$ is the freestream velocity, with U_{Vb} and U_{Vf} the velocity vortices relative to the body, and the velocity of vortices relative to the freestream at the separation point, respectively. Finally, D_S is the drag due to the vortex wake.

From 6.5,

$$C_{D_S}a = C_D D \Rightarrow C_{D_S} \frac{U_{Vb}}{f} = C_D D \Rightarrow C_{D_S} \frac{U_{Vb}}{U_\infty} = C_D \frac{fD}{U_\infty} \Rightarrow C_{D_S} \frac{U_{Vb}}{U_\infty} = C_D \, St.$$

Again, noting that $U_\infty = U_{Vb} + U_{Vf}$ gives

$$C_{D_S} \left(1 - \frac{U_{Vf}}{U_\infty}\right) = C_D \, St. \tag{6.6}$$

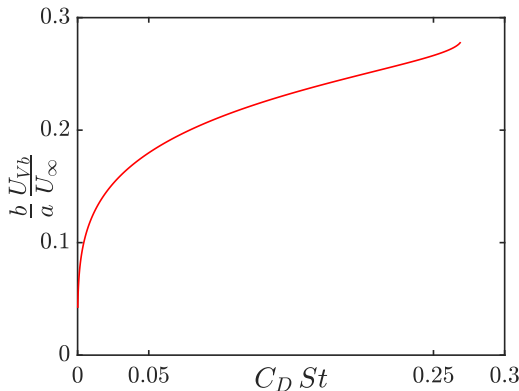Kronauer's stability criterion states that for a given U_{Vf}/U_∞, the aspect ratio,

Figure 20. Relationship between $\frac{bU_{Vb}}{aU_\infty}$ and $C_D\,St$ evaluated from the Kronauer's stability criterion.

b/a of the resulting vortex street is the one that corresponds to the minimum drag coefficient,

$$\frac{\partial C_{D_S}}{\partial\left(\frac{b}{a}\right)} = 0. \tag{6.7}$$

From 6.4 and 6.7,

$$2\cosh\frac{\pi b}{a} = \left(\frac{U_\infty}{U_{Vf}} - 2\right)\sinh\frac{\pi b}{a}\left(\cosh\frac{\pi b}{a}\sinh\frac{\pi b}{a} - \frac{\pi b}{a}\right). \tag{6.8}$$

To summarise, there are three unknown parameters so far, C_{D_S}, U_{Vf}, (b/a). Equations 6.4, 6.6, and 6.8 can be used to solve for these unknowns. Given the product $C_D\,St$, $\frac{bU_{Vb}}{aU_\infty}$ can thus be estimated. The variation of $\frac{bU_{Vb}}{aU_\infty}$ for a range of $C_D\,St$ is given in the figure 20 and this relationship forms equation 3.4.

$$\frac{b}{a}\frac{U_{Vb}}{U_\infty} = F\left(C_D\,St\right).$$

Thus, measurements of C_D, St and C_{P_b} can be used to evaluate the Bearman number St_B,

$$St_B = \frac{b}{a}\frac{U_{Vb}}{U_\infty}\frac{1}{(1 - C_{P_b})^{0.5}}.$$

6.4. *Velocity profiles in the wake of rough cylinders*

Figure 21(a) and (b) give the mean and fluctuating velocity profiles, respectively, for the $k_s/D = 1.9 \times 10^{-3}$ cylinder near the cylinder surface. While mean velocity increases steeply through the shear layer, fluctuating velocity increases, reaches a peak and then decreases. Since the difference in Reynolds number is small, there appears to be no significant difference in the mean and fluctuating velocity profiles between the two Reynolds numbers. The shear layer is slightly wider for the higher Reynolds number indicating that there was longer growth and hence slightly earlier separation. This observation is supported by the trends observed in θ_w previously.

Figures 21(c) and (d) give the mean and fluctuating profiles respectively at the same Reynolds number for varying roughness. For a given Reynolds number, an

increase in roughness leads to a wider shear layer (ascertained from the fluctuating velocity profile) at the same position downstream of the cylinder, implying an earlier separation for larger roughness. Figures 21(*e*) and (*f*) give the mean and fluctuating profiles respectively at the same Roughness Reynolds number for varying roughness. It is evident that the velocity profiles are very similar, further reinforcing that the separation angle and hence, the shear layer and wake width close to the body of the cylinder post-separation is similar for different roughness at the same Roughness Reynolds number. This also agrees with the previous observation of the Strouhal number collapse with Roughness Reynolds number.

Figure 22 gives the velocity distribution further downstream of the cylinder. As mentioned previously, owing to the limited range of Reynolds numbers tested for a given roughness, the differences in the wake between the two Reynolds numbers are almost insignificant. On the other hand, for a given Reynolds number, a decrease in roughness increases the velocity deficit and wake width close to the cylinder. This velocity deficit also diffuses faster for the smoother cylinder than that of the rougher cylinder indicating a faster velocity recovery. Mean and fluctuating velocity profiles are similar for different roughnesses at the same roughness Reynolds number, especially beyond 3 diameters downstream of the cylinder.
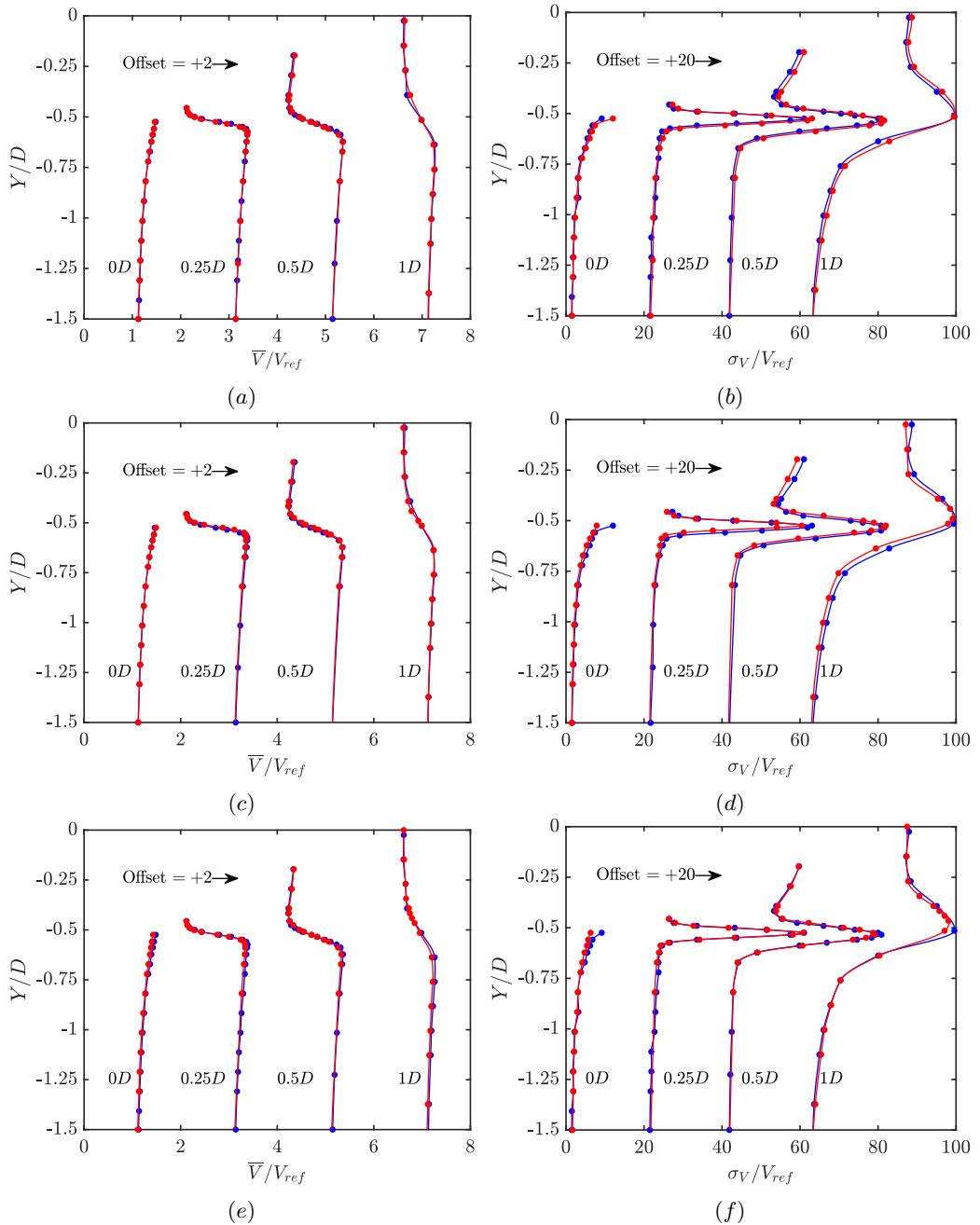
Anil Pasam et al.

Figure 21. Mean and fluctuating Velocity profiles downstream of the cylinder. (a) and (b): $k_s/D = 1.9 \times 10^{-3}$ at ——: $Re = 2.9 \times 10^5$ and ——: $Re = 3.8 \times 10^5$, (c) and (d): $Re \sim 3.8 \times 10^5$ over ——: $k_s/D = 1.9 \times 10^{-3}$ and ——: $k_s/D = 1.1 \times 10^{-3}$, and ($e$) and ($f$): $Re_{k_s} \sim 530$ over ——: $k_s/D = 1.9 \times 10^{-3}$ and ——: $k_s/D = 1.1 \times 10^{-3}$.
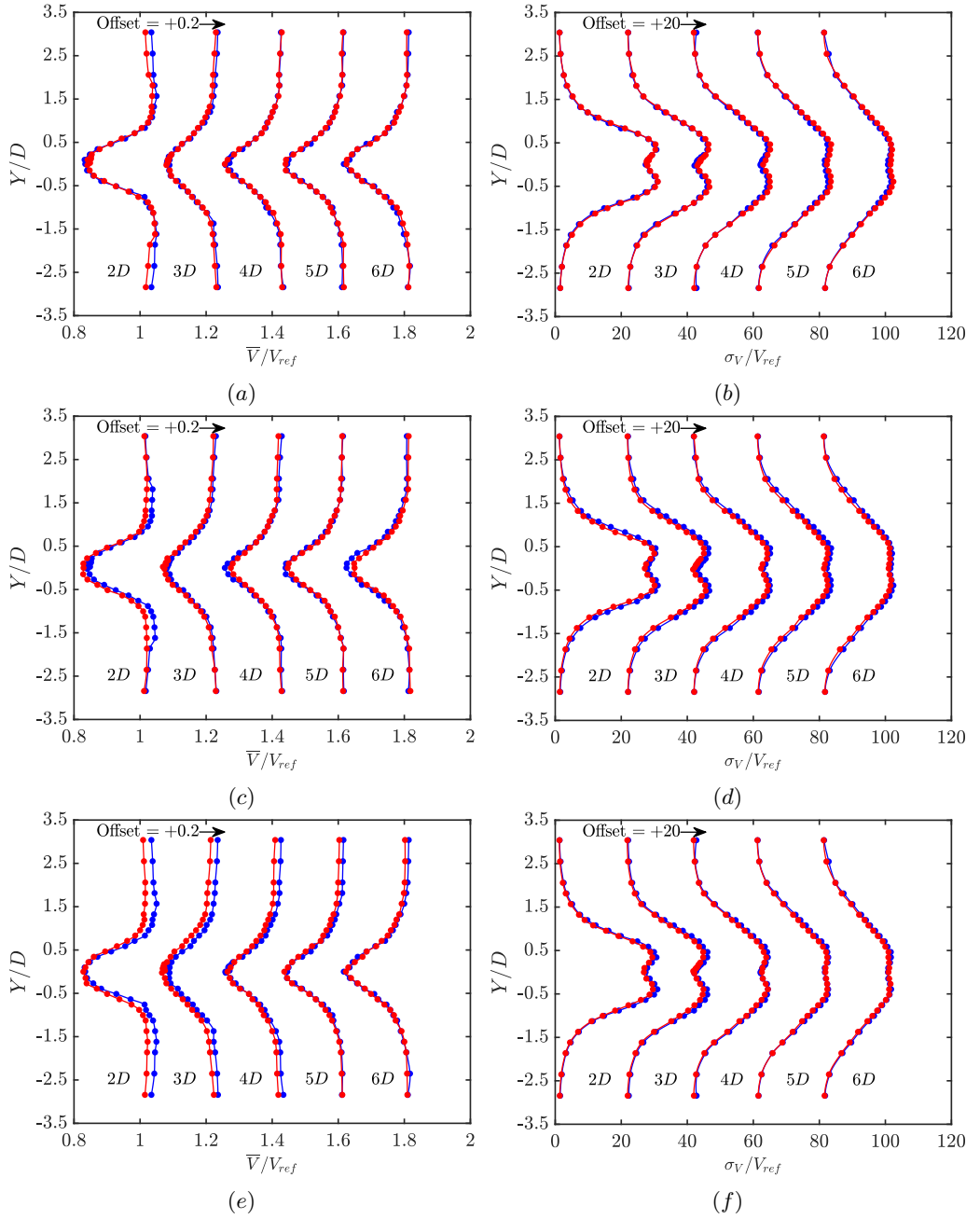
Figure 22. Mean and fluctuating Velocity profiles downstream of the cylinder. (a) and (b): $k_s/D = 1.9 \times 10^{-3}$ at ——: $Re = 2.9 \times 10^5$ and ——: $Re = 3.8 \times 10^5$, (c) and (d): $Re \sim 3.8 \times 10^5$ over ——: $k_s/D = 1.9 \times 10^{-3}$ and ——: $k_s/D = 1.1 \times 10^{-3}$, and ($e$) and ($f$): $Re_{k_s} \sim 530$ over ——: $k_s/D = 1.9 \times 10^{-3}$ and ——: $k_s/D = 1.1 \times 10^{-3}$.